communications physics

A Nature Portfolio journal

Article

https://doi.org/10.1038/s42005-025-02121-1

Divertor shaping with neutral baffling as a solution to the tokamak power exhaust challenge

Check for updates

Kevin Verhaegh[1,2] ✉, James Harrison[1], David Moulton[1], Bruce Lipschultz[3], Nicola Lonigro[1,3], Nick Osborne[1,4], Peter Ryan[1], Christian Theiler[5], Tijs Wijkamp[2,6], Dominik Brida[7], Cyd Cowley[1,3], Gijs Derks[2,6], Rhys Doyle[8], Fabio Federici[9], Bob Kool[2,6], Olivier Février[5], Antti Hakola[10], Stuart Henderson[1], Holger Reimerdes[5], Andrew Thornton[1], Nicola Vianello[11], Marco Wischmeier[7], Lingyan Xiang[1], the EUROfusion Tokamak Exploitation Team* & the MAST Upgrade Team*

Exhausting power from the hot fusion core to the plasma-facing components is one fusion energy's biggest challenges. The MAST Upgrade tokamak uniquely integrates strong containment of neutrals within the exhaust area (divertor) with extreme divertor shaping capability. By systematically altering the divertor shape, this study shows the strongest evidence to date to our knowledge that long-legged divertors with a high magnetic field gradient (total flux expansion) deliver key power exhaust benefits without adversely impacting the hot fusion core. These benefits are already achieved with relatively modest geometry adjustments that are more feasible to integrate in reactor designs. Benefits include reduced target heat loads and improved access to, and stability of, a neutral gas buffer that 'shields' the target and enhances power exhaust (detachment). Analysis and model comparisons shows these benefits are obtained by combining multiple shaping aspects: long-legged divertors have expanded plasma-neutral interaction volume that drive reductions in particle and power loads, while total flux expansion enhances detachment access and stability. Containing the neutrals in the exhaust area with physical structures further augments these shaping benefits. These results demonstrate strategic variation in the divertor geometry and magnetic topology is a potential solution to one of fusion's power exhaust challenge.

Sustainable nuclear fusion is one of the most promising solutions for the world's energy challenges, offering an essentially limitless and clean energy source. However, one of the critical hurdles in developing viable fusion reactors is efficiently managing its power exhaust: removing heat and particles from the hot fusing core while reducing surface heat fluxes to sufficiently low levels to prevent damaging the reactor's components[1,2]. Combining experiments, analysis and model results from the MAST Upgrade tokamak, this study not only demonstrates that innovative shaping of the power exhaust region can solve this critical challenge, but also explains the physics and synergy between combining different power exhaust shaping strategies.

In magnetic confinement fusion, such as tokamaks and stellarators[3], the hot fusion core plasma is confined within nested magnetic field lines ('closed flux tubes'). Heat and particles are expelled from the core into the edge region, where they follow the 'open flux tubes' forming the Scrape-Off Layer (Fig. 1a). Coils enable altering the magnetic topology of these open flux tubes to create a magnetic null point ('X-point'), which diverts heat and particle fluxes to a dedicated region called the 'divertor' (Fig. 1b). Since the power exhaust is carried by charged particles following the flux surfaces, the narrow width of the SOL results in extreme heat fluxes (150 MW m^{-2} for the DEMO reactor design[1,2]) due to the narrow plasma wetted area, far exceeding engineering limits (5–10 MW m^{-2} [1,2]) if unmitigated.

[1]United Kingdom Atomic Energy Authority, Culham, UK. [2]Eindhoven University of Technology, Eindhoven, The Netherlands. [3]York Plasma Institute, University of York, York, UK. [4]University of Liverpool, Liverpool, UK. [5]Swiss Plasma Centre, École Polytechnique Fédérale de Lausanne, Lausanne, Switzerland. [6]Dutch Institute for Fundamental Energy Research DIFFER, Eindhoven, The Netherlands. [7]Max Planck Institute for Plasma Physics, Garching, Germany. [8]Dublin City University, Dublin, Ireland. [9]Oak Ridge National Laboratory, Oak Ridge, TN, USA. [10]VTT Technical Research Centre of Finland, Espoo, Finland. [11]Consorzio RFX, Padova, Italy. *Lists of authors and their affiliations appears at the end of the paper. ✉e-mail: k.h.a.verhaegh@tue.nl

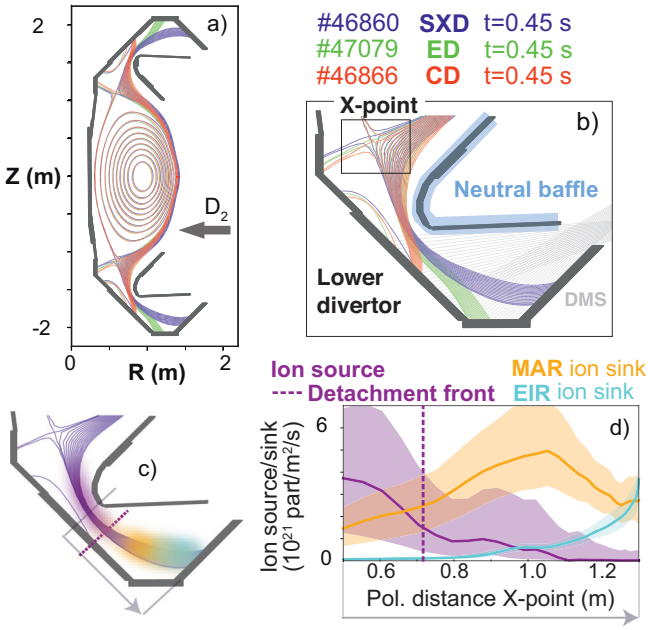

Fig. 1 | Overview of MAST-U plasma shapes and divertor processes. a Overview of the magnetic geometry for the Super-X Divertor (SXD[34], blue), Elongated Divertor (ED, green) and Conventional Divertor (CD, green), from the indicated discharges/times together with the fuelling (D_2) location and first wall geometry. **b** Lower divertor with diagnostic coverage of the Divertor Monitoring Spectrometer (DMS, grey)[8,40], X-point position and neutral baffle location (shaded cyan). **c** Schematic illustration of the characteristic processes in a detached MAST-U Super-X divertor featuring the ion source (magenta), Molecular Activated Recombination (MAR) ion sink (orange) and Electron Ion Recombination (EIR) ion sink (cyan). **d** Measured 1D profile of the schematic divertor processes in (**c**), obtained from line-integrated spectroscopic inferences (# 46860 at 45% Greenwald fraction[34]) (ions m^{-2} s^{-1}) as function of poloidal distance from the X-point to the target, indicated with a grey arrow in both **c** and **d**. The detachment (or ionisation) front position is indicated with a dotted magenta line in both **c** and **d**. The experimental results in (**d**) are derived from a probabilistic sample obtained from a Bayesian spectroscopic analysis, showing the median (solid lines) and the 68% equal-tailed confidence interval (shaded region). See 'Methods' section for more information about the analysis and uncertainty propagation.

To reduce target heat loads, the power must be spread over a larger area. This is first achieved by injecting radiating impurity gasses or hydrogen fuel to cool the divertor plasma and convert the heat carried by charged particles into heat carried by photons (radiation) that do not follow the magnetic field lines and thus dissipate the power volumetrically[4]. However, cooling the divertor plasma increases the ion target fluxes and associated power loading from surface recombination, limiting the total possible power reduction to a factor ~4[5]. 'Divertor detachment' is a process that reduces the ion target flux, enabling further power dissipation and order-of-magnitude target heat flux reductions[4–7]. At electron temperatures of ≤~3–5 eV, the ionising plasma 'detaches' from the target, forming a neutral buffer below the ionising plasma or 'detachment'/ionisation front (Fig. 1c, d). Plasma-atom/molecule interactions, within that buffer, cause simultaneous power, particle (e.g. ion), and momentum losses, that collectively drive detachment (see Methods section). Recombining the ions into neutral atoms, through ion sinks like Molecular Activated Recombination (MAR) and Electron-Ion Recombination (EIR) (Fig. 1c, d), plays a critical role in detachment[5–8]. One drawback of detachment is that it can be highly sensitive to changes in core power, impurity seeding and fuelling. A high sensitivity could more easily result in a loss of detachment, damaging the reactor walls, or in the detached region reaching the hot fusing core, resulting in a radiative collapse of the plasma[9] that can catastrophically damage a reactor[10]. Therefore, we refer to reducing the detachment sensitivity as an increased detachment stability for simplicity.

Despite advances in understanding and maximising the mitigation of heat/particle fluxes through plasma detachment, maintaining core performance while effectively exhausting power remains a major challenge and key uncertainty for future reactors[2]. Compact reactor designs like STEP[11,12], SPARC[13], ST-F1/E1[14] and ARC[15,16], aiming to accelerate the pathway to fusion energy[14,15], face even larger power exhaust challenges. Innovative power exhaust solutions are thus required for compact fusion reactors[11,13,16] and, as risk mitigation, for DEMO and beyond[17–19]. This includes (combinations of) liquid metal targets[20,21], high impurity injection to induce X-point radiators[22–24], and Alternative Divertor Configurations (ADCs)[25–27]. ADCs use coils to optimise the divertor magnetic topology to reduce heat loads whilst maintaining a hot fusion core[25]; increase the range of core conditions for which detachment can be achieved[25] and improve the stability of detachment[28] (see 'Methods' section).

One promising ADC approach combines long-legged divertors[27,29], achieved by increasing the distance between the X-point and the target to increase the power dissipation volume, with using the divertor magnetic topology to spread the power over a larger target area: poloidal and total flux expansion. Poloidal flux expansion increases the distance between poloidal magnetic flux tubes (poloidal flux expansion $F_x = \frac{B_\theta^u B_\phi^t}{B_\theta^t B_\phi^u}$ see Methods), whereas total flux expansion increases the magnetic field gradient by increasing the target radius (total flux expansion $F_R = \frac{B_t}{B_{xpt}}$). ADCs can be further optimised by containing the neutral particles within the divertor chamber using baffle plates (Fig. 1a), boosting plasma-neutral interactions and preventing neutrals escaping to the core where they cool the fusion core plasma, thus enhancing core-edge compatibility[29,30].

MAST Upgrade is the UK's national fusion experiment, newly built to tackle fusion's power exhaust challenge. MAST-U's design uniquely integrates strong neutral baffling, long-legged divertors ((poloidal) divertor leg length/major radius >1), and high total flux expansion (up to 2.5). In contrast, conventional divertor solutions (on JET, Asdex-Upgrade[31]) have short-legged divertors (divertor leg length/major radius <0.1), negligible total flux expansion (F_R ~ 1) and no neutral baffles. The spherical ('apple-shaped') nature of MAST-U enables F_R variations over a much larger range (1–2.5) than possible in conventional ('doughnut-shaped') tokamaks with flexible shaping, such as TCV (1–1.6)[25]. Preliminary MAST-U results under low power (Ohmic) conditions (P_{SOL} = 0.4 MW) demonstrate the benefits of the 'Super-X Divertor' (SXD)[32,33], which has the highest F_R achievable, over the conventional divertor (F_R = 1.2)[8,34,35]; consistent with simulations[35].

This work shows the key experimental results of exploring alternative divertor solutions on MAST-Upgrade. Since there is a continuum of ADC solutions, this work studies the impact of varying total flux expansion and divertor leg length instead of focusing only on the Super-X topology, using plasmas with higher power (1.5–1.7 MW Neutral Beam Injection (NBI) heating, P_{SOL} = 1.2 MW). This not only provides the strongest experimental evidence to date for the benefits of ADCs to our knowledge by combining total flux expansion, divertor leg length and neutral baffling; but also shows these benefits are maintained at more moderate divertor shaping (lower F_R and shorter leg lengths than the maximum values). These power exhaust benefits are obtained without any adverse core impact and include target heat flux reductions; improved access to, and stability of, plasma detachment; as well as improved core-edge compatibility. Since engineering complexity is a critical hurdle for integrating ADCs in reactors, the finding that their benefits can be maintained at more moderate shaping is of key importance for fusion reactor engineering and design[18,19], advancing the path for using ADCs to achieve sustainable fusion energy.

Low temperature plasma physics and plasma chemistry are central to plasma detachment. In this work we unravel these processes as a function of divertor shape through advanced analysis techniques[8] and model comparisons. This shows insights into how different shaping aspects work together to achieve the observed benefits. The divertor poloidal leg length/volume results in additional power/particle losses without impacting the plasma upstream ('Volume long-legged divertors drives power and particle

Table 1 | Summary of divertor magnetic shape parameters

Discharge	R_t (m)	F_x	F_R	L (m)	L_{pol} (m)	Description
46860	1.45	9	2.3	19	1.3	Super-X Divertor (SXD)
47079	1.11	6	1.7	17	1.1	Elongated Divertor (ED)
46762	0.79	3.3	1.2	13	0.64	Conventional Divertor (CD)
46895	0.81–1.39	4–6	1.2–2.2	13–19	0.65–1.3	CD ->ED ->SXD scan

Target radius (R_t), poloidal flux expansion (F_x), total flux expansion (F_R), connection length from the upstream midplane to the target (L) and poloidal leg length from the X-point to the target (L_{pol}) for the discharges studied. Discharge # 46895 keeps the core density and power constant as the divertor topology is changed over the range of the first three discharges.

losses' section). Total flux expansion improves access to, and stability of, detachment ('Total flux expansion improves detachment access and stability' section). Strong neutral baffling enables total flux expansion benefits and augments plasma-neutral interactions, maximising the benefits of divertor poloidal leg length ('Neutral trapping enables power exhaust shaping benefits' section). This improves our understanding of how divertor shaping can improve power exhaust in agreement with reduced model predictions ('Total flux expansion improves detachment access and stability' section) and simulations ('Exhaust simulations' section), further advancing the path for using ADCs to achieve sustainable fusion energy.

Results

By systematically comparing three divertor geometries: the Conventional Divertor (CD); Elongated Divertor (ED) and Super-X Divertor (SXD) (Fig. 1, divertor shape parameters shown in Table 1), we obtain five benefits of combined total flux expansion, poloidal leg length and divertor neutral baffling.

(i) Improved access to detachment: detachment occurs at lower core density.
(ii) Increased operational regime for detached divertor operation: the range of core density and powers at which the divertor detached is larger.
(iii) Improved detachment stability: the sensitivity of detachment to changes in core density is reduced.
(iv) Reduced target heat fluxes and power loads.
(v) Improved power exhaust without adverse core impact: core performance in detached conditions is improved.

For each divertor configuration, the evolution of their power exhaust and detachment properties are diagnosed as the core electron density is gradually increased and the divertor conditions grow colder, whilst other parameters are held as constant as possible. For ease of reference and for comparison against literature, the line-averaged core electron density (obtained from interferometry) is expressed as a fraction to the maximum core density, Greenwald, limit[36] which depends on the plasma current and tokamak size.

Power exhaust benefits

The longer legged, totally flux expanded, divertors have improved access to detachment at lower core plasma densities. In the CD, the integrated target particle fluxes (Fig. 2a) increase as function of core density, indicative of an attached divertor plasma, up to a core Greenwald fraction of $f_{GW} \approx 40\%$. At this point, both the particle flux at the target decreases and the ionisation front detaches from the target (Fig. 2b), indicative of the onset of detachment. In contrast, the ED and SXD are detached throughout the scanned core density range: the particle flux does not increase with increasing density whilst the ionisation front remains detached. Since there is no difference in the density limit achievable between the different geometries, the operational window (in terms of the core density range for which the discharge is detached) for detached operation is increased for the long-legged divertors compared to the CD.

The longer-legged, totally flux expanded, divertors have a higher detachment stability to quasi-steady-state changes in core parameters, qualitatively consistent with reduced (steady-state) models ('Detachment Location Sensitivity (DLS) model' section[28]). The sensitivity of the detachment front to changes in core density, i.e, the slope of the detachment front position (Fig. 2b) is a factor 5 steeper for the CD ($f_{GW} \approx 40\%$), compared to the ED and SXD at this core density: the detachment front is much more sensitive to changes in core density for the CD. These steady-state results indicate an inherent stabilisation, akin to a shock absorber, of the detachment front for the ED and SXD, in contrast to the CD where the ionisation region moves with minimal core changes out of the divertor chamber after detachment, increasing core and X-point radiation (Fig. 2h). Although the reduced detachment sensitivity and increased operational window of detachment are related, they are not identical. Using the analogy of a shock absorber, a reduced detachment sensitivity (enabled by total flux expansion) corresponds to a stronger damping, whereas the wider detached operational regime (enabled by poloidal leg length combined with total flux expansion) increases the displacement the spring can undergo before the elastic limit is exceeded: both work in unison enhancing detachment stability for long-legged, totally flux expanded divertors.

These benefits extend to dynamic variations in fuelling[37] and heating perturbations[34]: indicating an inherent lesser response of the detachment location to fuelling/heating transients and improved detachment control for the ED and SXD[37]. In contrast to our quasi-steady-state experiments, these dynamic variations feature more than seven times faster fuelling changes to which the divertor responds dynamically[37].

The longer-legged, totally flux expanded, divertors result in larger heat flux reductions than expected. Based on the magnetic geometry[25], a reduction in perpendicular heat flux by ~5.8× and ~2.1× for the SXD and ED is expected, compared to the CD, mainly due to increased poloidal (F_x ~3.0 × (SXD) and ~1.6× (ED)) and total (F_R ~2.0 × (SXD) and ~1.4× (ED)) flux expansion. However, a much larger reduction in target heat flux is observed: ~18.5× and ~7 × for the SXD and ED, compared to the CD (Fig. 2c). The longer-legged divertors result in additional heat flux dissipation through volumetric and/or radial/cross-field transport by a factor ~3.2× , qualitatively consistent with both SOLPS-ITER simulations ('Exhaust simulations' section)[35] and volumetric power loss estimates ('Volume long-legged divertors drives power and particle losses' section).

The longer-legged, totally flux expanded, divertors enable divertor detachment without adverse core impact, in contrast to the CD - which needs high densities to detach (f_{GW} >40%). The core densities, temperatures and P_{SOL} are similar for the CD, ED and SXD (Fig. 2d–h). These results indicate a strong decoupling between the divertor shape and the obtained core conditions, even when the outer target is detached.

After having shown the benefits of strongly baffled, long-legged, totally flux-expanded, divertors, we will explore why these divertor configurations have a superior exhaust performance using spectroscopic analysis[38], reduced models and simulation comparisons. This shows poloidal leg length, total flux expansion and strong neutral baffling strengthen each other's impact and all work together to achieve the observed benefits. The additional leg volume in the SXD and ED, compared to the CD, results in their superior power dissipation and drives the reduction of the ion target flux during detachment through ion sinks, whereas total flux expansion drives reductions in detachment onset and improves detachment front stability. Neutral baffling augments plasma-neutral interactions, strengthening the benefits of poloidal leg length, and

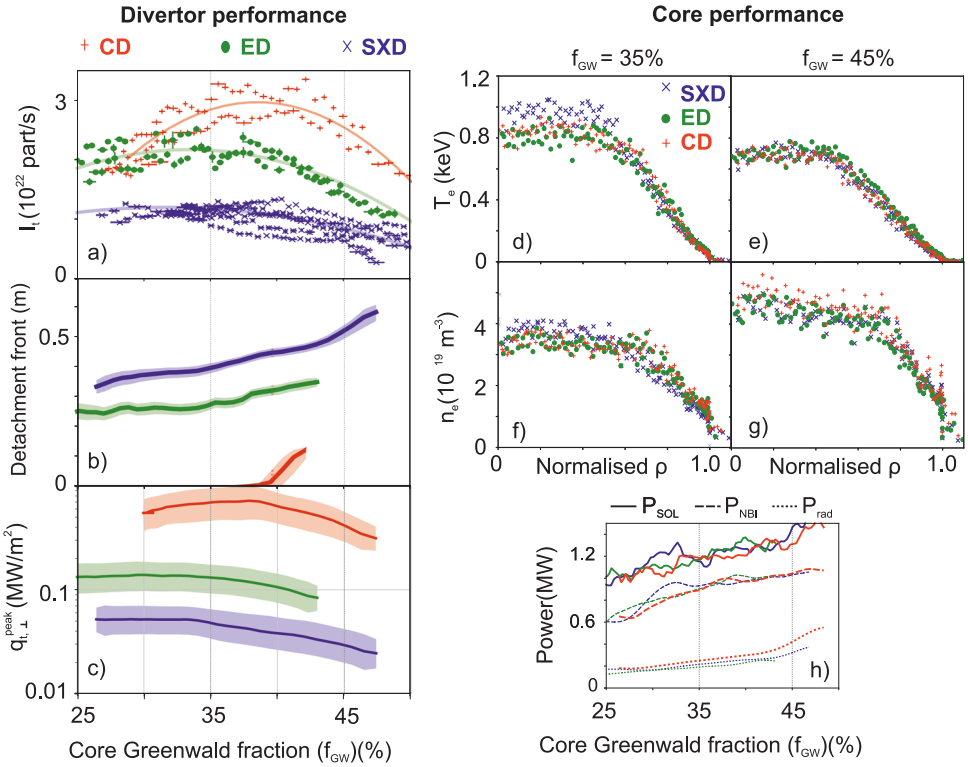

Fig. 2 | Improved divertor performance without adverse impact core for long-legged divertors. Comparison of divertor (**a**, **b**, **c**) and core (**d**, **e**, **f**, **g**, **h**) performance as function of core Greenwald fraction (f_{GW} in %) for the CD (red), ED (green) and SXD (blue). Divertor parameters: **a** Integrated ion target flux (symbols) (with polynomial fits (solid, shaded line)), **b** detachment (ionisation) front position as poloidal distance to the target, **c** estimated perpendicular target heat load on a logarithmic scale, combining Langmuir probe and spectroscopy measurements (see Methods)[8,40]. The results in (**b** and **c**) are derived from a probabilistic sample obtained from a Bayesian spectroscopic analysis, showing the median and the 68% equal-tailed confidence interval (shaded region). See 'Methods' section for more information about the analysis and uncertainty propagation. Core parameters: **d**–**g** core electron temperatures and densities at two different core Greenwald fractions (corresponding to vertical dotted lines in (**a**, **b**, **c**, **h**)) indicated by blue crosses (SXD), green dots (ED) and red plusses (CD), **h** P_{SOL} (solid lines) deduced from the following contributors: NBI absorption (TRANSP, dashed lines); Ohmic heating (EFIT, not shown); changes to stored energy (EFIT, not shown) and core radiative losses (bolometry, dotted lines).

enables total flux expansion benefits by preventing neutral leakage to the core.

Volume long-legged divertors drives power and particle losses

Particle balance analysis shows increased ion sinks reduce the target fluxes in the SXD and ED compared to the CD (Fig. 3a–c), whereas the total ion source is the same within uncertainties for all three different geometries. Ion sinks are significant in both the SXD and the ED from the start of those discharges, both through MAR as well as EIR (in the SXD). Our spectroscopic analysis reveals plasma conditions of $n_e = 2\text{–}4 \times 10^{19}\,m^{-3}$ and $T_e \approx 0.2$ eV in the region where EIR becomes observable ($f_{GW} > 33\%$ in the SXD and $f_{GW} > 40\%$ in the ED)[34,39]. MAR only appears in the CD at the highest core densities after its ionisation front detaches from the target ($f_{GW} > 40\%$), but its magnitude remains limited downstream the baffle.

The total ion source, inferred through particle balance, is obtained by adding the ion target flux and the ion sinks observed in the divertor chamber (see Methods section). This consists out of the divertor chamber ion source and any net inflow of ions into the divertor chamber. The ion source is generated between the X-point, predominantly downstream the most upstream-end of the baffle ($|Z| = 1.3$ m, Fig. 1): the neutral baffling is effective in limiting the ion source upstream of the X-point for all three configurations, consistent with simulation results ('Exhaust simulations' section). However, only up to 40% of the total ion source is generated downstream the most downstream-end of the baffle ($|Z| = 1.55$ m, Fig. 1) in the divertor chamber[34].

Analogously to the particle flux reduction, it is the additional volumetric power dissipation in their divertor volume (Fig. 3d–f) that drives the reduction in target power loads for the SXD and ED. The inferred power flowing into the divertor chamber is similar for all three geometries (Fig. 3d–f for f_{GW} <40%). As the inferred hydrogenic radiation is similar to the total measured radiation from an imaging bolometer (not shown)[40], the divertor chamber power losses mostly arise from hydrogenic processes. These hydrogenic power losses reduce P_{target} by a factor ~×4 (SXD) and ~×2 (ED) compared to the CD; consistent with the target heat load reduction being larger than expected based on geometry (Fig. 2c). A significant part of the ED and SXD hydrogenic power losses originate in the detached regime from Molecular Activated Dissociation (MAD). Elastic collisions between the plasma and the neutral cloud, which is neglected above, can further augment the power losses in the ED and SXD through radial transport of neutrals by up to 15% of P_{SOL}[41] according to the SOLPS-ITER simulations shown in 'Exhaust simulations' section. This would occur in the detached region and depend on the plasma-neutral interaction volume downstream the ionisation front, highlighting the benefits of increased divertor leg length[41].

The ED and SXD maintain strong radiation in the divertor chamber. That is in contrast to the CD configuration where the radiation upstream of the divertor baffle lowers P_{div} after the detachment onset ($f_{GW} > 40\%$), consistent with the much higher detachment front location sensitivity to changes in the core density (Fig. 2b). These results illustrate longer-legged divertors can 1) increase maximum (divertor) power dissipation; 2) maintain power losses away from the X-point towards the divertor target; and 3) further enhance power losses after the onset of detachment.

The impact of divertor shaping on power and particle exhaust is revealed when studying the 1D profiles of ion sources and sinks (a–c), as well as power flows (g), along the divertor leg as function of poloidal distance to the X-point at a fixed core density ($f_{GW} = 35\%$) (Fig. 4). Both profiles are similar between the different geometries (up until the CD detachment onset) at the same poloidal distance to the X-point: the plasma is thus predominantly altered in the extended region. The deeper detachment and lower power loads in the SXD and ED are brought on by interactions in the additional volume available downstream of the ionisation region when the divertor leg is extended. Plasma-chemistry occurring in this region, resulting in MAR and MAD, plays a key role explaining the differences between the different divertor geometries.

Total flux expansion improves detachment access and stability

To gain further insights into the impact of divertor shaping on detachment, the experimental results are compared against the DLS analytical

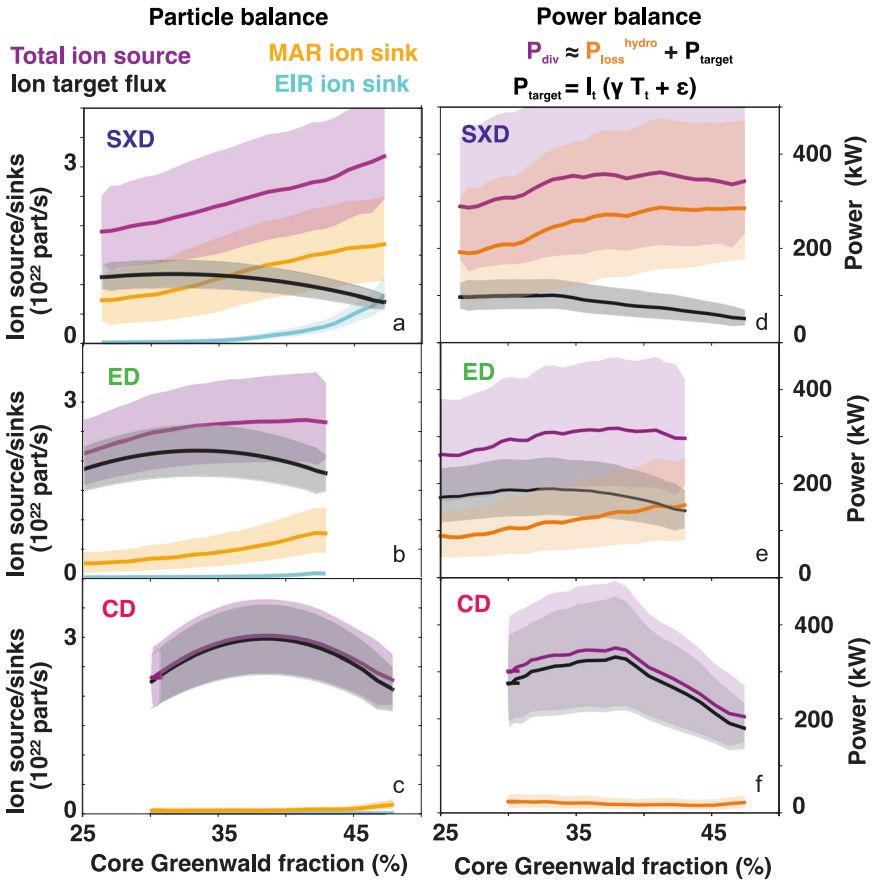

Fig. 3 | Power and particle balance shows additional volume long-legged divertor drives power and particle losses. Particle (**a**–**c**) and power (**d**–**f**) balance comparisons between different divertor shapes as function of core Greenwald fraction. **a**–**c** Particle balance showing the ion target flux (lower outer divertor) - black, total ionisation source - magenta, Molecular Activated Recombination (MAR - orange) and Electron-Ion Recombination (EIR - cyan) ion sinks (both ion sinks are integrated over the divertor chamber) for the Super-X Divertor (SXD) (**a**), Elongated Divertor (ED) (**b**) and Conventional Divertor (CD) (**c**). **d**–**f** Power balance showing hydrogenic power losses P_{loss}^{hydro} (orange, integrated over the divertor chamber), target power deposition P_{target} (black, obtained from spectrocopically inferred temperatures and Langmuir probe particle fluxes) and estimated power flow into the divertor chamber (magenta, $P_{div} \approx P_{loss}^{hydro} + P_{target}$) assuming that the divertor chamber power losses are dominantly hydrogenic, in agreement with imaging bolometry measurements[34]. Under the assumption that the lower and upper divertors are similar (consistent with Langmuir probe results[34]), P_{div}, P_{loss}^{hydro} and P_{target} have been multiplied by two to obtain integrated values of the upper and lower outer divertors. The results are derived from a probabilistic sample obtained from a Bayesian spectroscopic analysis, showing the median and the 68% equal-tailed confidence interval (shaded region). See Methods section for more information about the analysis and uncertainty propagation.

model[28,42,43]. The DLS model predicts detachment occurs if the parameters driving detachment (in our case core density (f_{GW}) and power (P_{SOL}), lumped together as $C \propto \frac{n_{e,u}\sqrt{f_t}}{q_{\parallel}^{5/7}} \propto \frac{f_{GW}}{P_{SOL}^{5/7}}$—see 'Methods' section) reaches the detachment threshold, C_t. C_t is a function of the magnetic geometry: $C_t \propto \frac{1}{F_R}\left(\frac{B_{xpt}}{<B>}\right)^{2/7} \frac{1}{L_{\parallel}^{2/7}}$, depending mostly on total flux expansion (F_R), connection length ($L_{\parallel}$, parallel to the field line) and the averaged magnetic field strength $<B>$. Total flux expansion and connection length both lower C_t, reducing the density (and impurity content - see Methods section) required for detachment at a fixed P_{SOL}.

The impact of total flux expansion on the detachment onset predicted by the DLS model is consistent with our observations (Table 2). The DLS predicted benefits for the SXD and ED over the CD arise mostly from an increase in total flux expansion. Given the density at which the CD detaches, the DLS predicts that the SXD and ED are already detached at the lowest core density achieved, consistent with the experiment. To compare the SXD and ED against each other, the onset of EIR is used as a colder reference point for DLS comparisons, showing agreement within 10% of the experiment. Furthermore, the DLS model predicts that the detachment front position only depends on the magnetic field topology upstream of the detachment front (see Methods section), consistent with the observed invariance of the upstream parameters to the downstream divertor magnetic topology.

Although only the magnetic geometry is used for obtaining DLS predictions on the differences between the SXD, ED and CD, it should be noted that the DLS model derivation assumes that: 1) the detachment front is infinitely thin; 2) all power dissipation is driven by impurity radiation. Both these assumptions are invalid for the MAST-U conditions shown, although the validity of these assumptions would increase in more reactor-relevant conditions. The agreement between the DLS model and the MAST-U results suggests, however, that the impact of divertor topology on the detachment onset may be more generally applicable outside of impurity radiation dominant conditions. Furthermore, the DLS model neglects radial heat transport, which may be enhanced due to total flux expansion[44]. Further work is required generalising the DLS model for MAST-U like conditions and investigating the impact of radial transport.

Our power and particle balance analysis showed the additional volume (or poloidal leg length) in the SXD and ED is critical to explain the reduction of power and particle loads during detachment. Total flux expansion, instead, drives 80% of the improved access to detachment according to DLS model comparisons, with the longer divertor leg length driving the remaining 20%. The DLS model also predicts that total flux expansion reduces detachment sensitivity, qualitatively consistent with ED and SXD observations (benefit iii): the combination of increasing divertor leg length/volume and total flux expansion result in strong, synergistic, power exhaust benefits.

Neutral trapping enables power exhaust shaping benefits

Although the poloidal divertor leg length downstream the baffle entrance is very different between the the different topologies, our experiments suggest that the baffling has a similarly strong impact on the CD (up until its detachment onset), ED and SXD. The observed and simulated ('Exhaust simulations' section) divertor neutral pressures are similar between the three geometries. Likewise, the neutral trapping, defined as the ratio between the ion source downstream the X-point to the total ion source[33], is similar between the three divertor topologies in simulations (78% for the SXD and ED and 75% for the CD, respectively), despite the SXD and ED configurations being deeply detached ('Exhaust simulations' section). In contrast, SOLPS-ITER simulations for a core density ramp of the (open, un-baffled) conventional TCV divertor indicated a neutral trapping of 32–45% in detachment onset conditions, decreasing during deeper detachment to

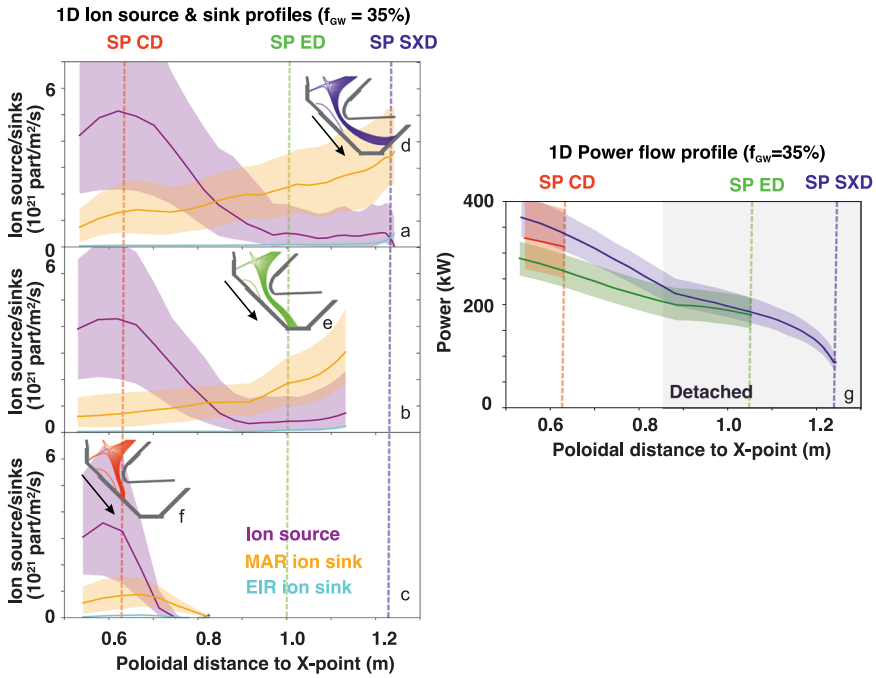

Fig. 4 | Power flow and 1D ion sources/sinks show similar divertor conditions at same poloidal distance to X-point. Spectroscopically inferred line-integrated ion sources (magenta) and sinks (Molecular Activated Recombination (MAR) - orange; Electron-Ion Recombination - cyan) (part. m^{-2} s^{-1}) for the Super-X (SXD) (**a**), Elongated (ED) (**b**) and Conventional (CD) (**c**) Divertors at f_{GW} = 35% as function of poloidal distance to the X-point. The red (CD), green (ED) and blue (SXD) vertical coloured dotted lines indicate their respective strike point positions, indicated by their magnetic geometry (**d**–**f**). The 1D ion source/sink profiles (**a**, **b**, **c**) are extended downstream of their respective strike-points due to convolution of the radial-extent of the SOL/far-SOL with the spectroscopic lines-of-sight, where the plasma is colder than at the separatrix. **g** Power flow (W) towards the divertor targets as function of poloidal distance to the X-point from the divertor entrance to the target for the CD (red), ED (green) and SXD (blue) at f_{GW} = 35%, with vertical dotted lines indicating their respective strike points. The part where the divertor leg is detached is shaded in grey in grey. The power flow is inferred by subtracting from P_{div} the cumulative sum of the hydrogenic power losses from upstream to the target. The results are derived from a probabilistic sample obtained from a Bayesian spectroscopic analysis, showing the median and the 68% equal-tailed confidence interval (shaded region). See Methods section for more information about the analysis and uncertainty propagation.

11%[33,45]. However, the increased detachment front sensitivity of the CD likely results in a reduction of neutral trapping after its detachment onset, diminishing the impact of neutral baffling on the CD after its detachment onset.

The benefits of long-legged divertors, total flux expansion, divertor shaping and neutral baffling have been individually studied on TCV[25,27]; showing benefits of neutral baffling[30,46–48] and long divertor leg lengths[27]. The benefits of total flux expansion (both in terms of detachment onset and front sensitivity/stability) were, however, much smaller than predicted by the DLS model[49,50]. Escape of neutrals from the divertor to the SOL upstream of the X-point can lead to strong plasma flows from the midplane to the target[51,52], which diminishes the impact of total flux expansion on the detachment onset[49]. SOLEDGE2D-EIRENE simulations suggest that the neutral baffling on TCV may be insufficient to recover the full benefit of total flux expansion[53], consistent with previous SOLPS-ITER simulations[33,54] which showed that the neutral trapping of the (open, unbaffled) TCV Super-X divertor was worse than that of the conventional divertor. This not only negates part of the benefits of total flux expansion due to an ion flow from upstream the X-point towards the target, but also reduces the benefit of the neutrals in power/particle dissipation between the Super-X divertor compared to the conventional divertor.

This difference between MAST-U and TCV, as well as the absence of strong flows from the midplane to the X-point in MAST-U simulations, suggests that strong neutral trapping, obtained by baffling on MAST-U, enables the shaping benefits of total flux expansion. Additionally, neutral baffling augments power/momentum/particle losses from plasma-neutral interactions such as MAR and MAD by containing the neutrals in the divertor chamber, amplifying the benefits of long-legged divertors ('Volume long-legged divertors drives power and particle losses' section). Neutral baffling is not required to obtain strong neutral trapping on high power devices (i.e., JET, AUG) near attached conditions as the neutral mean-free-paths are decreased, leading to a shorter extent of the ionisation region. However, baffling would still be required to maintain high neutral trapping in cases where the ionisation source is significantly upstream of the target, motivating the STEP[55], SPARC[13] and ARC[16] divertor designs. The MAST-U results suggest that neutral baffling can be placed downstream the X-point - the results suggest the baffle structure should be: 1) upstream of the intended location of the ionisation front; 2) sufficiently prohibiting the escape of neutrals to the SOL.

Table 2 | DLS reduced model predictions are in agreement with observations

	Detachment onset		EIR onset	
	Model	Experiment	Model	Experiment
SXD	−55%	<−37%	0%	Reference
ED	−40%	<−37%	+36%	+27%
CD	0%	Reference	+106%	>+52%

Measured and Detachment Location Sensitivity (DLS) model predicted relative differences (in core density) between the different divertor topologies (Super-X (SXD), Elongated (ED) and Conventional (CD) Divertor) for the detachment onset (T_e = ~3–5 eV) and the onset of Electron Ion Recombination (EIR), serving as a colder reference point ($T_e \ll 1$ eV). The experimentally observed density at which the CD detaches ($f_{GW}^{ref,CD,detach}$) and at which the EIR occurs in the SXD ($f_{GW}^{ref,SXD,EIR}$) are used as reference densities. The percentages shown are the observed and DLS modelled relative density differences to the reference for detachment onset ($f_{GW}^{ED,SXD,detach}/f_{GW}^{ref,CD,detach}$) and EIR onset ($f_{GW}^{CD,ED,EIR}/f_{GW}^{ref,SXD,EIR}$). These DLS modelled differences only depend on magnetic topology, see Methods section. The density range obtainable in the experiment limits the differences in detachment and EIR onset that can be explored between the different topologies. Therefore, when < (or >) is indicated, the detachment or EIR onset is not observed in the experiment and the relative difference is larger than indicated.

Exhaust simulations

MAST-U[56] uniquely integrates strong baffling and extreme levels of total flux expansion. The DLS detachment onset predictions (C_t) vary by 110% between the MAST-U CD and SXD. Comparatively, C_t varies by 70% for a range of TCV divertor geometries (target radius scan, poloidal flux

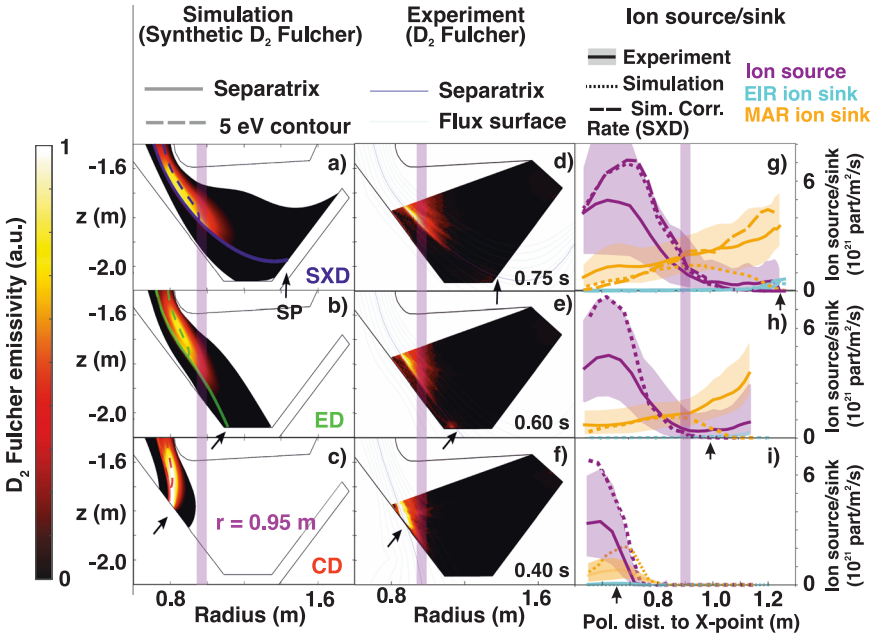

Fig. 5 | Increasing the divertor leg length does not alter the ionisation region after detachment, in agreement with simulations. Synthetic D_2 Fulcher emission from SOLPS-ITER simulations for the Super-X (SXD) (**a**, blue), Elongated (ED) (**b**, green) and Conventional Divertors (CD (**c**, red), overlaid with 5 eV contours (dashed lines) and the separatrix (solid line). **d**–**f** Experimentally measured D_2 Fulcher band emission (595-605 nm) for a strike point scan with magnetic equilibrium shown, moving from CD to SXD at constant density and power, obtained through inverting Multi-Wavelength-Imaging (MWI) imaging data for # 46895[57]. **g**–**i** 1D ion sources and sinks (ionisation - magenta, Molecular Activated Recombination (MAR) ion sink - magenta, Electron-Ion Recombination (EIR) ion sink - cyan), obtained from spectroscopic analysis integrated along the spectroscopic lines of sight (Fig. 1b) (part. m^{-2} s^{-1}), compared against synthetic diagnostic results from SOLPS-ITER simulations (dotted lines). For the SXD (**g**) two SOLPS-ITER simulation results are shown: one with default rates and one with corrected molecular charge exchange ($D_2 + D^+ \rightarrow D_2^+ + D$) rates ('Sim. Corr. Rate'), obtained from[34], which increases MAR. To guide the eye, a shaded magenta vertical line has been added at a radius of 0.95 m and a black arrow has been added at the strike point location (**a**–**i**). The experimental results in (**g**, **h**, **i**) are derived from a probabilistic sample obtained from a Bayesian spectroscopic analysis, showing the median (solid lines) and the 68% equal-tailed confidence interval (shaded region). See Methods section for more information about the analysis and uncertainty propagation.

expansion scan, as well as for the X-point target divertor)[25,27]. By integrating strong baffling, long-legged divertors and total flux expansion, MAST-U retrieves the full benefit of its shaping capability on the detachment onset and stability (factor 5 × reduced sensitivity for ED and SXD vs CD, Fig. 2b), as well as power and particle exhaust capability. We will now investigate the results of a single discharge under constant constant core density (30% Greenwald fraction, $n_e^{sep} \approx 0.8 \times 10^{18} m^{-3}$) and power ($P_{SOL} \approx 1.0$ MW), where C_t was altered by 110% by slowly sweeping the outer strike point from a CD to an ED to a SXD geometry. No significant differences are observed, at the same strike point position and core density, during this strike point scan at constant core density with the density ramps presented previously.

The results in Fig. 2b suggested that the ionisation front position, once detached from the target, is invariant to the magnetic topology downstream of it: its location depends only on the upstream magnetic topology. This is confirmed by the strike point sweep discharge, where the core conditions remain mostly unchanged, with a 5-10% increase in upstream and core T_e when transitioning from CD to SXD (potentially due to the longer connection length[4]). After the D_2 Fulcher band emission front, which is a proxy for the ionisation front[8,57,58], detaches from the target (target radius ≈0.95 m), it remains close to this radial position as the strike point is swept further and further outwards and both total flux expansion and poloidal leg length is increased (Fig. 5d–f). This implies that the ionisation front position (for this P_{SOL} and f_{GW}) remains at a constant poloidal distance to the X-point as the divertor leg length is further increased.

This behaviour agrees with SOLPS-ITER predictions[35] of the CD, ED and SXD configurations (Fig. 5a–c). The CD simulation is attached, whereas the SXD and ED simulations are detached. The radius of both the D_2 Fulcher emission front as well as the 5 eV contour, for the ED and SXD, remains near $r = 0.95$ m. The D_2 Fulcher emission near the X-point region is also in agreement between experiments (Fig. 6), suggesting that the strong neutral trapping obtained in the simulations is consistent with the experiment. However, the simulations feature an attached inner target (Fig. 6a–c) with strong D_2 Fulcher emission near the inner strike point (Fig. 6d–f), which is not observed experimentally (Fig. 6g–i). This suggests the inner target power loading is negligible in the experiments and overestimated in SOLPS-ITER simulations. This requires further study including using multi-diagnostic, Bayesian, to infer plasma parameters outside the divertor chamber analysis techniques[59].

SOLPS-ITER simulations suggest radial plasma transport is driven primarily in the ionising regime and is thus similar between the three different divertor shapes, whilst radial heat transport from neutrals occurs downstream of it[35]. This seems consistent with 2D emissivity and electron density measurements[60], which is to be studied in more detail in future work using more attached conditions and multi-diagnostic techniques to infer 2D plasma parameters[59].

A more detailed comparison between experiments and simulations is obtained by comparing their ion sources and sinks (Fig. 5g-i) in the outer divertor chamber, indicating a quantitative agreement between experiments and simulations for the ion source and EIR. The MAR ion sinks are underestimated in the simulation in the detached region. This discrepancy is resolved when a corrected rate for molecular charge exchange[34] is used in SOLPS-ITER (Fig. 5g).

Discussion

Using the unique capabilities of MAST-U as a test bed for investigating alternative divertor topologies reduces uncertainty in extrapolating current knowledge to reactor class devices by validating both reduced models and exhaust simulations: a crucial milestone for exploring ADCs as a reactor solution. There are, however, key differences between MAST-U and a reactor that must be addressed.

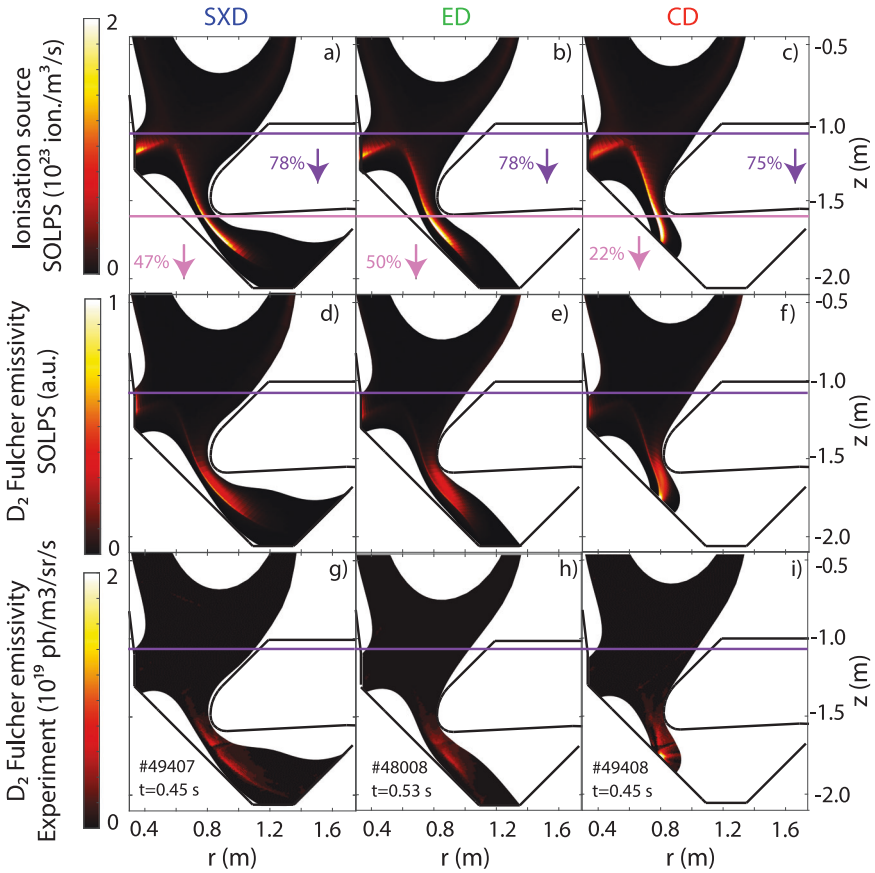

Fig. 6 | Overview of simulated and experimental ion sources and D_2 Fulcher emission for different divertor shapes. a–c 2D ionisation source from SOLPS-ITER simulations (shown in Fig. 5) with horizontal lines at $z = -1.6$ m (pink) and $z = 1.07$ m (magenta), demarking the edge of the divertor spectroscopy view and X-point, respectively. The fraction of the ion source downstream these limits compared to the total ion source (outer leg only) are noted. **d–f** Synthetic diagnostic for the D_2 Fulcher emissivity (arbitrary units) obtained from SOLPS-ITER simulations. **g–i** Measured D_2 Fulcher emissivity (595-605 nm) obtained from combined divertor imaging[57] and X-point imaging inversions. The indicated time and discharges used are shown and are obtained from repeat discharges for the same core density as used in Fig. 5. A horizontal line at the height of the X-point location is added (magenta). Only emissivities obtained at the same r, z corresponding to the simulation grids are shown. An inversion artefact is present near $r = 0.85$ m, $z = -1.6$ m, where there is a gap in coverage between the X-point and divertor imaging systems. Data are shown for the Super-X (SXD, blue, **a**,**d**,**g**), Elongated (ED, green, **b**,**e**,**h**) and Conventional (CD, red, **c**,**f**,**i**) Divertors.

First, reactors will operate at higher power input and smaller heat flux widths than MAST-U. As a result, heat loads will become so large that impurity seeding will be required to lower target temperatures sufficiently to enable detachment. Understanding how combining total flux expansion, divertor neutral baffling, and poloidal leg length affects impurity-driven power dissipation requires further investigation. Reactor-scale simulations have, however, demonstrated that ADCs enhance power dissipation, enabling operation with target heat fluxes below engineering limits with reduced impurity concentrations[11,16,17].

Although higher power conditions shorten neutral mean-free-paths - impacting neutral transport, plasma-molecular interactions are expected to play a key role in obtaining significant power, momentum and particle dissipation during (deep) detachment according to exhaust simulations that incorporate long-legged, tightly baffled, divertors[11,34,41]. The critical role plasma-molecular chemistry plays in the ED and SXD illuminated discrepancies with simulations (Fig. 5h) that have been reduced with improved rates for $D_2 + D^+ \rightarrow D_2^+ + D$. Extrapolating these improved rates to reactors with long-legged, tightly baffled, divertors shows they can make a critical impact on the reactor scale[34].

Secondly, reactor-grade operation typically involves H(igh confinement)-mode operation. Current H-mode operation exhibits violent ELMs that result in extremely high heat loads. Although reactors will aim to minimise or suppress ELMs, it remains unclear whether ADCs can effectively mitigate the heat loads of residual (fast, ELM) transients to increase divertor lifetimes.

Thirdly, our MAST-U results show a balanced double-null configuration, with similar particle fluxes reaching the lower and upper outer divertors and negligible power reaching the inner target (Fig. 6). Achieving such up/down balance in reactors poses challenges due to a larger distance between the X-point and poloidal field coils and smaller scrape-off-layer widths[12] (10–12 mm for the current MAST-U experiments; 1–2 mm for STEP[55] and 0.2–0.4 mm for SPARC[13]). Although the exhaust benefits of double null may be limited according to reactor exhaust simulations[61] and TCV experiments[50], double-null imbalances exacerbates inner target power loading and may necessitate solutions for spherical tokamak reactors, such as a proposed inner target X-Divertor geometry[11,55] requiring further experimental validation.

One concern of outer target optimisation strategies is that the increased outer target connection length will exacerbate the inner target heat load in single null conditions in attached conditions according to reduced models[62]. This was in contrast to detached DEMO Super-X divertor simulations, which indicated inner target heat loads were reduced with outer divertor optimisation[17,19], requiring further study.

This reduced model (for attached conditions) predicts an increase of inner target heat loads by 31% (ED) and 57% (SXD) compared to the CD. However, these increased inner target heat loads are reduced when accounting for outer target detachment. Using the ED and SXD outer divertor detachment front as a virtual target, the predicted additional inner target heat loads are reduced below 15% compared to an outer target attached CD.

Future MAST-U experiments aim to address these key differences and advance towards more reactor-relevant scenarios. Planned upgrades include increased external heating from 4.4 MW to over 10 MW (>2026), enabling hotter, more attached divertor conditions. Cryopumping has been installed to reduce divertor neutral pressures and obtain hotter divertor conditions (2025). Advanced scenario development (2025) may enable enable single-to-double-null comparisons. Preliminary results suggest that the benefits of ADCs observed in this study persist in H-mode and may even buffer small ELMs, requiring further investigation[40].

Overall, our results demonstrate that ADCs not only improve exhaust performance, enabling reduced upstream density and likely thus impurity concentration/core radiation in reactors[17], but also improve core-edge compatibility when paired with strong baffling. This allows for detached divertor operation without compromising core conditions: a major

milestone towards proving the applicability of ADCs in reactors. However, any reactor design needs a compromise between engineering complexity and attractive operating regimes[18,19]. The increased engineering complexity of some ADCs, such as the Super-X divertor, remains a significant consideration for reactor designs due to associated cost, space constraints and magnetic control tolerances[18,19]. Our findings underscore that smaller modifications to divertor topology, such as transitioning from CD to ED, can achieve significant performance gains that are consistent with reduced model predictions and exhaust simulations. ADC design is therefore a continuum—an insight that has implications for reactor designs of DEMO, as well as more compact machines (SPARC, ARC, STEP)[13,16,55], and paves the way for designs that optimise power exhaust and core-edge compatibility with reduced engineering and integration demands[18,19].

Methods

MAST upgrade, alternative divertor configurations and the super-X divertor

MAST Upgrade is the UK's national fusion experiment tackling one of fusion energy's biggest challenges: plasma exhaust. It is a medium sized, small aspect ratio (i.e., spherical) tokamak (major radius: 0.9 m, minor radius: 0.6 m) operated by the United Kingdom Atomic Energy Authority[56,63]. It has a toroidal field of 0.8 T, its plasma current can reach up to 1 MA, and features one off-axis and one on-axis neutral beam injector for external heating, of up to 2.2 MW each. TRANSP simulations are used to model the neutral beam absorption, required to estimate the power entering the scrape-off-layer (SOL). MAST-U features core Thomson scattering to obtain core electron density and temperature profiles, uses far-infrared-reflectometry (FIR) to obtain the line-averaged electron density and utilises the magnetic equilibrium reconstruction code EFIT++ to reconstruct the magnetic equilibria based on magnetic probe measurements. Its divertor is well diagnosed, featuring line-of-sight spectroscopy[8], imaging diagnostics[57], Langmuir probes[64], as well as an imaging bolometry system at the X-point[65].

In this work, fuelling injection from the low field side of the core plasma is used to maintain L-mode conditions whilst controlling the core density in real time by adapting the low-field side main chamber fuelling rate[66]. The advantage of using higher power L-mode conditions in this study is that the upstream density can be reduced compared to that in H-mode. This makes the plasma less detached and enables a wider range of upstream density scans to investigate the evolution during detachment[34].

MAST-U features upper and lower divertor chambers, enabling double null diverted scenarios. The divertor chambers prevent neutral transport from the divertor to the core, providing neutral baffling and contributing to core-edge compatibility. The large divertor chamber, combined with various divertor coils[56], facilitates the integration of complex divertor shapes with strong neutral baffling. This enables studying the impact of divertor shaping on power exhaust while maintaining strong neutral baffling.

With this shaping flexiblity, MAST-U can alter the poloidal flux expansion, connection length and total flux expansion. Poloidal flux expansion, $F_x = \frac{B_\theta^u B_\phi^t}{B_\theta^t B_\phi^u}$[25]), is the ratio of the perpendicular flux surface spacing at the target and upstream, where $B_{\theta,\phi}^{u,t}$ are the poloidal (θ) and toroidal (ϕ) components of the magnetic field at upstream (u) and at the target (t), respectively. Increasing F_x reduces the target heat loads (W m^{-2}) by spreading it over a larger surface. Increasing the connection length between the midplane and the divertor target ($L_\parallel$), provides a larger radiating volume and is expected to improve power exhaust[25]. Total flux expansion ($F_R = \frac{B_{xpt}}{B_t}$) increases the cross-sectional area of a flux tube, spreading the heat over a larger radius and lowering the target temperature[25,28]. The spherical nature of MAST-U enables varying total flux expansion over an unprecedented range to the best of our knowledge, making it an ideal testbed for studying the impact of total flux expansion in a strongly baffled divertor.

Divertor detachment, ion source/sink inferences and power balance

Power exhaust can be facilitated by plasma detachment, which is a state where simultaneous power, particle and momentum losses result in a simultaneous reduction of target particle fluxes and plasma target temperature.

Using hydrogen atomic Balmer line spectroscopic analysis[5,8], the electron temperature, ion sources (I_i) and sinks (I_r) from plasma-atom and molecular interactions, as well as the hydrogenic radiative power losses and Molecular Activated Dissociation, can be inferred from the hydrogen Balmer line emission.

Since the line-of-sight spectroscopy system has a set fan of views throughout the divertor leg (Fig. 1), spatial profiles of chordally integrated ion sources and sinks (part. m^{-2} s^{-1}) along the divertor leg can be obtained (Fig. 3d–f). During detachment, first the ionisation source detaches from the target ($T_e < 3$–5 eV, inferred spectroscopically[8]) and ultimately Electron-Ion Recombination (EIR) starts to occur near the target ($T_e \approx 0.2$ eV, $n_e \approx 2$–4×10^{19}m^{-3}, according to spectroscopic inferences of the high-n ($n > 9$) Balmer line spectra[40]). By tracking the location of the downstream-end of the ionisation source ($(1.5 \pm 0.25) \times 10^{21}$ part. m^{-2} s^{-1}) and the upstream-end of the EIR sink ($(3 \pm 0.5) \times 10^{20}$ part. m^{-2} s^{-1}), the distance between the target and the ionisation front (defined as the detachment front) and EIR front (colder reference point of deeper detachment) can be obtained. These numbers are obtained as onset points based on the spatial profiles of ion sources and sinks presented in Fig. 1d.

Combining spectroscopic inferences on ion sources and sinks with Langmuir probe measurements, information on both particle and power balance can be obtained. The total ion target flux (I_t in part. s^{-1}) is obtained by integrating the ion target flux Γ_t (part. m^{-2} s^{-1}) measured by Langmuir probes. From conservation of particles, the total ion target flux should equal the ion sources minus the ion sinks, in addition to any net ion inflow into the monitored system I_u, Eq. (1). Using particle balance, the total ion source ($I_i + I_u$) can be inferred (Eq. (1)).

$$I_t = I_i - I_r + I_u \tag{1}$$

The target power loading can be inferred using a combination of spectroscopy and Langmuir probe measurements. To overcome limitations of estimating target temperatures using Langmuir probes in low temperature conditions[64], spectroscopy from lines-of-sight closest to the target is used to infer a characteristic target electron temperature T_t. Using this temperature, the perpendicular plasma target power deposition can be estimated as $P_{\perp,\text{target}} = I_t(\gamma T_t + \epsilon)$ (in W), whereas the peak perpendicular heat flux can be estimated as $q_{\perp,\text{peak}} = \Gamma_{t,\text{peak}}(\gamma T_t + \epsilon)$ (in W m^{-2}). A sheath transmission factor of $\gamma = 7$ is assumed (valid for equal electron and ion temperatures) and both surface recombination and molecular re-association is accounted for in the potential energy $\epsilon = 13.6 + 2.2$ eV.

Assuming that all volumetric power losses are purely due to hydrogenic radiation as well as dissociation, which is motivated by the observation that hydrogenic radiation estimates from spectroscopic analysis align with the measured total radiation in these conditions[34], the power into the divertor chamber can be estimated by summing $P_{\perp,\text{target}}$ and the inferred hydrogenic divertor radiative power loss. This ignores power transfer from the plasma to the neutral cloud through elastic collisions, which can become substantial in the SOLPS-ITER simulations shown (up to 15% of P_{SOL}[41]), in qualitative agreement with the observed rotational D_2 rotational temperatures[41].

Although this does include surface recombination, it does not include target heat loads due to photons and neutral atoms. Including dissociation as a total loss channel implies assuming that the neutral atoms, after dissociation, are mostly lost to the side walls, rather than reaching the target (and hence do not contribute as target heating), which is consistent with findings in SOLPS-ITER simulations.

Detachment Location Sensitivity (DLS) model

The DLS analytical model[28,42,43] can model the impact of the magnetic divertor geometry on the detachment threshold in terms of changes to a control parameter $C \propto \frac{n_u \sqrt{f_z}}{q_\parallel^{5/7}}$, which depends on upstream density n_u, impurity fraction f_z and parallel heat flux $q_\parallel$. The detachment onset C_t is proportional to a term that only depends on the magnetic geometry[43], as shown in Eq. (2). In here, B is the total magnetic field, ξ is the coordinate representing the volume of the flux tube between the target and a given position along the divertor leg, scaled by a reference area $\propto 1/B_{xpt}$.

$$C_t \propto \frac{B_t}{B_{xpt}^{3/7}} \times \left(\int_t^{xpt} B^2(\xi) d\xi + \int_{xpt}^{u} B^2(\xi) \left(\frac{L-\xi}{L-\xi_{xpt}} \right) d\xi \right)^{-2/7} \quad (2)$$

The advantage of this formulation is that it considers the full magnetic field dependency numerically, rather than approximating the field variation as linear with ξ. Under those approximations, Eq. (2): $C_t \propto \frac{B_t}{B_{xpt}} \left(\frac{B_{xpt}}{<B>}\right)^{2/7} \frac{1}{L_\parallel^{2/7}}$[42]. The DLS model thus predicts that detachment onset is facilitated by increased connection length ($L_\parallel$) and increased total flux expansion $\frac{B_t}{B_{xpt}}$. We find negligible differences between this approximate form and the full numerical calculation for the MAST-U shapes reported in this work. The DLS model is applied to a flux tube that is 0.5 mm outwards of the separatrix into the SOL, to avoid numerical errors. Instead of finding the detachment onset, where a 'thermal front' (i.e., detachment front) leaves the target, Eq. (2) can also be applied to any position of the detachment front along the leg by changing the target to a different location. This implies that the front location only depends on the magnetic geometry upstream of the front. By monitoring how quickly the front position changes along the divertor leg, the DLS can make predictions on detachment front sensitivity.

The DLS model formally assumes that all power is dissipated by impurity radiation and that the radiating specie has a constant concentration in the radiating region. In the MAST-U divertor chamber, the power is not dissipated by impurity radiation: the radiative power losses are dominated by hydrogenic interactions[8] consistent with SOLPS-ITER modelling predictions[35]. Impurity radiation could, however, be significant upstream of the divertor chamber entrance[8,34]. However, the impact of the divertor topology on the detachment onset appears to be more generally applicable outside of impurity radiation dominant conditions.

Assuming the impurity fraction is constant and that the upstream electron density and heat flux are proportional to, and fully determined by, f_{GW} and P_{SOL}, the detachment threshold is expected to be dependent on f_{GW} and P_{SOL}. There is a small variation in P_{SOL} during the experiment (increased NBI power absorption at higher densities), which is accounted for in our predictions. In our detached conditions, λ_q cannot be monitored from target measurements. However, scaling laws on MAST (attached, open, conventional divertor) did show an increase in λ_q at higher f_{GW}[67] and this scaling law dependency is accounted for in our predictions. Not accounting for this predicted change in λ_q and for P_{SOL} changes only has a secondary impact on the predicted f_{GW} for the various detachment threshold and does not impact any of the conclusions in this work.

Exhaust simulations—SOLPS-ITER

Reduced models, such as the DLS model, are useful for building a physics understanding. However, the divertor behaviour is highly complex: it is a 2D/3D phenomena that involves interactions between the plasma with neutral atoms and molecules. SOLPS-ITER is a state-of-the-art code suite for advanced power exhaust modelling[68]. It combines a fluid code (B2.5) with a Monte Carlo neutral code that tracks the neutrals and incorporates several atomic and molecular databases (Eirene)[68].

Interpretive SOLPS-ITER simulations have been performed using a baseline Super-X SOLPS-ITER setup that has been matched against Ohmic experimental data[35]. These simulations have been extrapolated to the higher power experiments presented here, using corresponding experimental magnetic equilibria for the Super-X, Elongated and Conventional divertors, fuelling location, and P_{SOL}. The fuelling rate has been tuned in order to match the experimentally measured upstream electron densities.

For the SOLPS-ITER simulation setup (Super-X divertor only) with corrected rates ('Sim. Corr. Rate (SXD)', Fig. 5g), the molecular charge exchange rate ($D_2 + D^+ \rightarrow D_2^+ + D$) has been replaced with a rate that has been specifically computed for deuterium[34]. This rate uses ab inito calculated cross-sections from ref. 69 and combines them with a collisional-radiative model calculation (to compute the vibrational distribution of H_2 molecules) utilising the same data (apart from molecular charge exchange) that is used in Eirene. Furthermore, it accounts for isotope mass differences correctly[34,45], as well as for the differences in vibrational energy levels between the different isotopes[34,69]. This improved rate is significantly increased at low temperatures ($T < 2$ eV), particularly for the heavier isotopes (i.e., deuterium, tritium), compared to the default rate used in Eirene[34,45].

Data availability

The data that support these studies are openly available at: [70]. This contains metadata further explaining the data. The data is provided in a zip file containing folders of: 1) general data on discharge parameters (Numpy files) (Fig. 2); 2) spectroscopic analysis results (Numpy files) (Figs. 1, 3, 4); 3) imaging (MWI) inversions (Numpy files) (Fig. 6); 4) Thomson scattering data (Matlab files) (Fig. 2); 5) SOLPS simulation and synthetic diagnostic results (Matlab files) (Fig. 6); 6) predictions from the DLS model (Table 2). To obtain further information on the data and models underlying this paper please contact publicationsmanager@ukaea.uk.

Code availability

Code and software used to generate the results in this paper are referenced in the metadata of the data availability DOI[70]. This contains links to git repositories that are used to access and process the data[71], as well as references to codes from other published works that have been used to process this data.

Received: 26 September 2024; Accepted: 2 May 2025;
Published online: 23 May 2025

References

1. Wenninger, R. et al. DEMO divertor limitations during and in between ELMs. *Nucl. Fusion* **54**, 114003 (2014).
2. Zohm, H. et al. The EU strategy for solving the DEMO exhaust problem. *Fusion Eng. Des.* **166**, 112307 (2021).
3. Effenberg, F. et al. First demonstration of radiative power exhaust with impurity seeding in the island divertor at Wendelstein 7-X. *Nucl. Fusion* **59**, 106020 (2019).
4. Stangeby, P. C. Basic physical processes and reduced models for plasma detachment. *Plasma Phys. Control. Fusion* **60**, 044022 (2018).
5. Verhaegh, K. et al. A novel hydrogenic spectroscopic technique for inferring the role of plasma–molecule interaction on power and particle balance during detached conditions. *Plasma Phys. Control. Fusion* **63**, 035018 (2021).
6. Lipschultz, B. et al. Ultrahigh densities and volume recombination inside the separatrix of the Alcator C-Mod tokamak. *Phys. Rev. Lett.* **81**, 1007–1010 (1998).
7. Krasheninnikov, S. I. & Kukushkin, A. S. Physics of ultimate detachment of a tokamak divertor plasma. *J. Plasma Phys.* **83**, 155830501 (2017).
8. Verhaegh, K. et al. Spectroscopic investigations of detachment on the MAST Upgrade Super-X divertor. *Nucl. Fusion* **63**, 016014 (2022).
9. Goetz, J. A. et al. Comparison of detached and radiative divertor operation in Alcator C-Mod. *Phys. Plasmas* **3**, 1908–1915 (1996).
10. Maris, A. D., Wang, A., Rea, C., Granetz, R. & Marmar, E. The impact of disruptions on the economics of a tokamak power plant. *Fusion Sci. Technol.* **80**, 636–652 (2024).

11. Hudoba, A., Newton, S., Voss, G., Cunningham, G. & Henderson, S. Divertor optimisation and power handling in spherical tokamak reactors. *Nucl. Mater. Energy* **35**, 101410 (2023).
12. Osawa, R. et al. SOLPS-ITER analysis of a proposed STEP double null geometry: impact of the degree of disconnection on power-sharing. *Nucl. Fusion* **63**, 076032 (2023).
13. Kuang, A. Q. et al. Divertor heat flux challenge and mitigation in SPARC. *J. Plasma Phys.* **86**, 865860505 (2020).
14. Windridge, M. Tokamak energy. In: Nuttall, W. J., Konishi, S., Takeda, S., Webbw-Wood, D. (editotrs) *Commercialising Fusion Energy*, 2053-2563, 5.1–5.15 (IOP Publishing, 2020).
15. LaBombard, B. et al. ADX: a high field, high power density, advanced divertor and RF tokamak. *Nucl. Fusion* **55**, 053020 (2015).
16. Wigram, M. R. K. et al. Performance assessment of long-legged tightly-baffled divertor geometries in the ARC reactor concept. *Nucl. Fusion* **59**, 106052 (2019).
17. Xiang, L. et al. The operational space for divertor power exhaust in DEMO with a Super-X divertor. *Nucl. Fusion* **61**, 076007 (2021).
18. Kembleton, R., Siccinio, M., Maviglia, F. & Militello, F. Benefits and challenges of advanced divertor configurations in DEMO. *Fusion Eng. Des.* **179**, 113120 (2022).
19. Militello, F. et al. Preliminary analysis of alternative divertors for DEMO. *Nucl. Mater. Energy* **26**, 100908 (2021).
20. Van Eden, G., Kvon, V., Van De Sanden, M. & Morgan, T. Oscillatory vapour shielding of liquid metal walls in nuclear fusion devices. *Nat. Commun.* **8**, 192 (2017).
21. Lore, J. D. et al. Simulation of liquid lithium divertor geometry using SOLPS-ITER. *IEEE Trans. Plasma Sci.* **50**, 4199–4205 (2022).
22. Stroth, U. et al. Model for access and stability of the X-point radiator and the threshold for marfes in tokamak plasmas. *Nucl. Fusion* **62**, 076008 (2022).
23. Pan, O. et al. SOLPS-ITER simulations of an X-point radiator in the ASDEX Upgrade tokamak. *Nuclear Fusion* **63**, 016001 (2022).
24. Lunt, T. et al. Compact radiative divertor experiments at ASDEX Upgrade and their consequences for a reactor. *Phys. Rev. Lett.* **130**, 145102 (2023).
25. Theiler, C. et al. Results from recent detachment experiments in alternative divertor configurations on TCV. *Nucl. Fusion* **57**, 072008 (2017).
26. Ryutov, D. D. & Soukhanovskii, V. A. The snowflake divertor. *Phys. Plasmas* **22**, 110901 (2015).
27. Reimerdes, H. et al. TCV experiments towards the development of a plasma exhaust solution. *Nucl. Fusion* **57**, 126007 (2017).
28. Lipschultz, B., L. Para, F. & Hutchinson, I. Sensitivity of detachment extent to magnetic configuration and external parameters. *Nucl. Fusion* **56**, 056007 (2016).
29. Umansky, M. et al. Study of passively stable, fully detached divertor plasma regimes attained in innovative long-legged divertor configurations. *Nucl. Fusion* **60**, 016004 (2019).
30. Reimerdes, H. et al. Initial TCV operation with a baffled divertor. *Nucl. Fusion* **61**, 024002 (2021).
31. Eich, T. et al. ELM divertor peak energy fluence scaling to ITER with data from JET, MAST and ASDEX upgrade. *Nucl. Mater. Energy* **12**, 84–90 (2017).
32. Valanju, P. M., Kotschenreuther, M., Mahajan, S. M. & Canik, J. Super-X divertors and high power density fusion devices. *Phys. Plasmas (1994-present)* **16**, 056110 (2009).
33. Fil, A. et al. Separating the roles of magnetic topology and neutral trapping in modifying the detachment threshold for TCV. *Plasma Phys. Control. Fusion* **62**, 035008 (2020).
34. Verhaegh, K. et al. Investigations of atomic and molecular processes of NBI-heated discharges in the MAST Upgrade Super-X divertor with implications for reactors. *Nucl. Fusion* **64**, 086050 (2024).
35. Moulton, D. et al. Super-X and conventional divertor configurations in MAST-U ohmic L-mode; a comparison facilitated by interpretative modelling. *Nucl. Fusion* **64**, 076049 (2024).
36. Greenwald, M. et al. A new look at density limits in tokamaks. *Nucl. Fusion* **28**, 2199 (1988).
37. Kool, B. et al. First demonstration of Super-X divertor exhaust control for transient heat load management in compact fusion reactors. Nat. Energy, in press. arXiv preprint (2025). arXiv:2407.07784.
38. Verhaegh, K. et al. The role of plasma-molecule interactions on power and particle balance during detachment on the TCV tokamak. *Nucl. Fusion* **61**, 106014 (2021).
39. Lonigro, N. et al. First 2D electron density measurements using multi-delay coherence imaging spectroscopy in the MAST-U Super-X divertor. *Plasma Phys. Control. Fusion* **67**, 035003 (2025).
40. Verhaegh, K. et al. The role of plasma-atom and molecule interactions on power and particle balance during detachment on the MAST Upgrade Super-X divertor. *Nuclear Fusion* (2023).
41. Osborne, N. et al. A novel understanding of the role of plasma-molecular kinetics on divertor power exhaust. ArXiv preprint (2024). arXiv:2410.14403.
42. Cowley, C., Lipschultz, B., Moulton, D. & Dudson, B. Optimizing detachment control using the magnetic configuration of divertors. *Nucl. Fusion* **62**, 086046 (2022).
43. Myatra, O. et al. Predictive SOLPS-ITER simulations to study the role of divertor magnetic geometry in detachment control in the MAST-U Super-X configuration. *Nucl. Fusion* **63**, 096018 (2023).
44. Brida, D. et al. Transport and profile broadening in the private flux region of ASDEX Upgrade and role for power exhaust. *Nucl. Fusion* **65**, 026065 (2025).
45. Verhaegh, K. et al. Investigating the impact of the molecular charge-exchange rate on detached SOLPS-ITER simulations. *Nucl. Fusion* **63**, 076015 (2023).
46. Raj, H. et al. Improved heat and particle flux mitigation in high core confinement, baffled, alternative divertor configurations in the TCV tokamak. *Nucl. Fusion* **62**, 126035 (2022).
47. Gorno, S. et al. Power exhaust and core-divertor compatibility of the baffled snowflake divertor in TCV. *Plasma Phys. Control. Fusion* **65**, 035004 (2023).
48. Sheikh, U. et al. Impact of the new TCV baffled divertor upgrade on pedestal structure and performance. *Nucl. Mater. Energy* **26**, 100933 (2021).
49. Carpita, M. et al. Parallel flows as a key component to interpret Super-X divertor experiments. *Nucl. Fusion* **64**, 046019 (2024).
50. Février, O. et al. Detachment in conventional and advanced double-null plasmas in TCV. *Nucl. Fusion* **61**, 116064 (2021).
51. Cowley, C., Moulton, D. & Lipschultz, B. Simulating the impact of baffling on divertor performance using SOLPS-ITER (2024). ArXiv pre-print. arXiv:2407.13501.
52. Havlickova, E. et al. SOLPS analysis of the MAST-U divertor with the effect of heating power and pumping on the access to detachment in the Super-X configuration. *Plasma Phys. Control. Fusion* **57**, 115001 (2015).
53. Meineri, C., Muscente, P., Theiler, C. & Galassi, D. Numerical study of fully baffled Super-X L-mode discharges on TCV. *Nucl. Mater. Energy* **34**, 101383 (2023).
54. Fil, A. M. D. et al. Identification of the primary processes that lead to the drop in divertor target ion current at detachment in TCV. *Contrib. Plasma Phys.* **58**, 746–750 (2017).
55. Henderson, S. et al. An overview of the STEP divertor design and the simple models driving the plasma exhaust scenario. *Nucl. Fusion* **65**, 016033 (2024).
56. Morris, W. et al. MAST Upgrade divertor facility: a test bed for novel divertor solutions. *IEEE Trans. Plasma Sci.* **46**, 1217–1226 (2018).

57. Wijkamp, T. et al. Characterisation of detachment in the MAST-U Super-X divertor using Multi-Wavelength Imaging of 2d atomic and molecular emission processes. *Nucl. Fusion* **63**, 056003 (2023).
58. Osborne, N. et al. Initial fulcher band observations from high resolution spectroscopy in the MAST-U divertor. *Plasma Phys. Control. Fusion* **66**, 025008 (2023).
59. Greenhouse, D. et al. Two-dimensional inference of divertor plasma characteristics: advancements to a Multi-Instrument Bayesian Analysis System. *Plasma Phys. Control. Fusion* **67**, 035006 (2025).
60. Lonigro, N. et al. 2D electron density profile evolution during detachment in Super-X divertor L-mode discharges on MAST-U (2024). ArXiv pre-print. arXiv:2410.00818.
61. Aho-Mantila, L. et al. Scoping the characteristics and benefits of a connected double-null configuration for power exhaust in EU-DEMO. *Nucl. Mater. Energy* **26**, 100886 (2021).
62. Maurizio, R. et al. Conduction-based model of the scrape-off layer power sharing between inner and outer divertor in diverted low-density tokamak plasmas. *Nucl. Mater. Energy* **19**, 372–377 (2019).
63. Harrison, J. R. et al. Benefits of the Super-X divertor configuration for scenario integration on MAST Upgrade. *Plasma Phys. Control. Fusion* **66**, 065019 (2024).
64. Ryan, P. J., Elmore, S. D., Harrison, J. R., Lovell, J. & Stephen, R. Overview of the Langmuir probe system on the Mega Ampere Spherical Tokamak (MAST) upgrade. *Rev. Sci. Instrum.* **94**, 103501 (2023).
65. Federici, F. et al. Design and implementation of a prototype infrared video bolometer (IRVB) in MAST upgrade. *Rev. Sci. Instrum.* **94**, 033502 (2023).
66. Derks, G. et al. Development of real-time density feedback control on MAST-U in L-mode. *Fusion Eng. Des.* **202**, 114387 (2024).
67. Harrison, J., Fishpool, G. & Kirk, A. L-mode and inter-ELM divertor particle and heat flux width scaling on MAST. *J. Nucl. Mater.* **438**, S375–S378 (2013).
68. Wiesen, S. et al. The new SOLPS-ITER code package. *J. Nucl. Mater.* **463**, 480–484 (2015).
69. Ichihara, A., Iwamoto, O. & Janev, R. K. Cross sections for the reaction $H^+ + H_2(\nu = 0 - 14) \rightarrow H + H_2^+$ at low collision energies. *J. Phys. B At. Mol. Optical Phys.* **33**, 4747–4758 (2000).
70. Verhaegh, K., Ryan, P., Wijkamp, T., Lonigro, N. & Moulton, D. Data set: "Experimental data and simulations comparing the divertor and core performance of the MAST upgrade Super-X, Elongated and Conventional Divertors in beam-heated L-mode conditions". UK Atomic Energy Authority, Open Data Registry (2024).
71. Verhaegh, K., Ryan, P., Wijkamp, T. & Lonigro, N. Accession codes for Data set: "Experimental data and simulations comparing the divertor and core performance of the MAST upgrade Super-X, Elongated and Conventional divertors in beam-heated L-mode conditions". Git repository (Zenodo) (2025).

Acknowledgements

This work has received support from EPSRC Grants EP/T012250/1, EP/N023846/1 and EP/W006839/1. This work is supported by US Department of Energy, Office of Fusion Energy Sciences under the Spherical Tokamak programme, contract DE-AC05-00OR22725. This work has been carried out within the framework of the EUROfusion Consortium, partially funded by the European Union via the Euratom Research and Training Programme (Grant Agreement No 101052200 – EUROfusion). The Swiss contribution to this work has been funded by the Swiss State Secretariat for Education, Research and Innovation (SERI). Views and opinions expressed are however those of the author(s) only and do not necessarily reflect those of the European Union, the European Commission or SERI. Neither the European Union nor the European Commission nor SERI can be held responsible for them.

Author contributions

Grouped co-authors indicate equal contributions.Kevin Verhaegh: Conceptualisation, Methodology, Software, Validation, Formal Analysis, Investigation, Data curation, Writing - Original Draft, Writing - Review & Editing, Visualisation, Supervision, Project Administration, Funding acquisition.James Harrison: Conceptualisation, Software, Resources, Writing - Review & Editing, Supervision, Funding Acquisition. David Moulton: Conceptualisation, Formal Analysis, Investigation, Writing - Review & Editing.-Bruce Lipschultz: Conceptualisation, Investigation, Supervision, Resources, Project administration. Nicola Lonigro: Investigation, Formal Analysis, Validation, Visualisation. Nick Osborne: Investigation, Validation. Peter Ryan: Formal Analysis, Validation, Visualisation. Christian Theiler: Conceptualisation, Investigation, Writing - Review & Editing, Project administration, Supervision, Funding acquisition. Tijs Wijkamp: Investigation, Formal analysis, Software, Visualisation, Writing - Review & Editing.Dominik Brida: Investigation, Project administration, Supervision, Funding acquisition. Cyd Cowley: Validation, Methodology. Gijs Derks: Investigation. Rhys Doyle: Investigation. Fabio Federici: Investigation, Writing - Review & Editing. Bob Kool: Investigation.Olivier Février Project administration, Funding acquisition. Antti Hakola: Conceptualisation, Project administration, Funding acquisition. Stuart Henderson: Investigation. Holger Reimerdes: Project administration, Funding acquisition. Andrew Thornton: Investigation. Nicola Vianello: Project administration, Funding acquisition, Supervision. Marco Wischmeier: Project administration, Funding acquisition, Supervision. Lingyan Xiang: Formal analysis.EUROfusion Tokamak Exploitation Team: Funding acquisition, Project administration, Resources. MAST Upgrade Team: Resources, Software, Data Curation, Project administration, Funding acquisition.

Competing interests

The authors declare no competing interests.

Additional information

Supplementary information The online version contains supplementary material available at https://doi.org/10.1038/s42005-025-02121-1.

Correspondence and requests for materials should be addressed to Kevin Verhaegh.

Peer review information *Communications Physics* thanks Yannik Marandet, Anthony Leonard and the other, anonymous, reviewer(s) for their contribution to the peer review of this work. A peer review file is available.

Reprints and permissions information is available at http://www.nature.com/reprints

Publisher's note Springer Nature remains neutral with regard to jurisdictional claims in published maps and institutional affiliations.

Open Access This article is licensed under a Creative Commons Attribution-NonCommercial-NoDerivatives 4.0 International License, which permits any non-commercial use, sharing, distribution and reproduction in any medium or format, as long as you give appropriate credit to the original author(s) and the source, provide a link to the Creative Commons licence, and indicate if you modified the licensed material. You do not have permission under this licence to share adapted material derived from this article or parts of it. The images or other third party material in this article are included in the article's Creative Commons licence, unless indicated otherwise in a credit line to the material. If material is not included in the article's Creative Commons licence and your intended use is not permitted by statutory regulation or exceeds the permitted use, you will need to obtain permission directly from the copyright holder. To view a copy of this licence, visit http://creativecommons.org/licenses/by-nc-nd/4.0/.

© The Author(s) 2025

the EUROfusion Tokamak Exploitation Team

D. Abate[11], J. Adamek[12], M. Agostini[11], C. Albert[13], F. C. P. Albert Devasagayam[14], S. Aleiferis[1], E. Alessi[15], J. Alhage[16], S. Allan[1], J. Allcock[1], M. Alonzo[17], G. Anastasiou[18], E. Andersson-Sunden[19], C. Angioni[7], Y. Anquetin[20], L. Appel[1], G. M. Apruzzese[17], M. Ariola[21], C. Arnas[22], J. F. Artaud[23], W. Arter[1], O. Asztalos[24], L. Aucone[25], M. H. Aumeunier[23], F. Auriemma[11], J. Ayllon[26], E. Aymerich[27], A. Baciero[28], F. Bagnato[5], L. Bähner[29], F. Bairaktaris[18], P. Balázs[24], L. Balbinot[11], I. Balboa[1], M. Balden[7], A. Balestri[5], M. Baquero Ruiz[5], T. Barberis[30], C. Barcellona[31], O. Bardsley[1], M. Baruzzo[17], S. Benkadda[20], T. Bensadon[32], E. Bernard[23], M. Bernert[7], H. Betar[33], R. Bianchetti Morales[1], J. Bielecki[34], R. Bilato[7], P. Bilkova[12], W. Bin[15], G. Birkenmeier[7], R. Bisson[22], P. Blanchard[5], A. Bleasdale[1], V. Bobkov[7], A. Boboc[1], A. Bock[7], K. Bogar[12], P. Bohm[12], T. Bolzonella[11], F. Bombarda[17], N. Bonanomi[7], L. Boncagni[17], D. Bonfiglio[11], R. Bonifetto[30], M. Bonotto[11], D. Borodin[35], I. Borodkina[12], T. O. S. J. Bosman[6], C. Bourdelle[23], C. Bowman[1], S. Brezinsek[35,36], D. Brida[7], F. Brochard[37], R. Brunet[23], D. Brunetti[1], V. Bruno[23], R. Buchholz[13], J. Buermans[38], H. Bufferand[23], P. Buratti[17], A. Burckhart[7], J. Cai[35], R. Calado[39], J. Caloud[12], S. Cancelli[25], F. Cani[40], B. Cannas[27], M. Cappelli[17], S. Carcangiu[27], A. Cardinali[17], S. Carli[41], D. Carnevale[42], M. Carole[20], M. Carpita[5], D. Carralero[28], F. Caruggi[25], I. Carvalho[1,43], I. Casiraghi[15], A. Casolari[12], F. J. Casson[1], C. Castaldo[17], A. Cathey[7], F. Causa[15], J. Cavalier[12], M. Cavedon[25], J. Cazabonne[5], M. Cecconello[19], L. Ceelen[6], A. Celora[25], J. Cerovsky[12], C. D. Challis[1], R. Chandra[14], A. Chankin[7], B. Chapman[1], H. Chen[26], M. Chernyshova[44], A. G. Chiariello[21], P. Chmielewski[44], A. Chomiczewska[44], C. Cianfarani[17], G. Ciraolo[23], J. Citrin[6], F. Clairet[23], S. Coda[5], R. Coelho[39], J. W. Coenen[35], I. H. Coffey[45], C. Colandrea[5], L. Colas[23], S. Conroy[19], C. Contre[5], N. J. Conway[1], L. Cordaro[11], Y. Corre[23], D. Costa[39], S. Costea[46], D. Coster[7], X. Courtois[23], C. Cowley[3], T. Craciunescu[47], G. Croci[25], A. M. Croitoru[47], K. Crombe[38], D. J. Cruz Zabala[26], G. Cseh[24], T. Czarski[44], A. Da Ros[23], A. Dal Molin[25], M. Dalla Rosa[25], Y. Damizia[1], O. D'Arcangelo[17], P. David[7], M. De Angeli[15], E. De la Cal[28], E. De La Luna[28], G. De Tommasi[21], J. Decker[5], R. Dejarnac[12], D. Del Sarto[33], G. Derks[6], C. Desgranges[23], P. Devynck[23], S. Di Genova[48], L. E. di Grazia[21], A. Di Siena[7], M. Dicorato[20], M. Diez[23], M. Dimitrova[12], T. Dittmar[35], L. Dittrich[29], J. J. Dominguez Palacios Durán[26], P. Donnel[23], D. Douai[23], S. Dowson[1], S. Doyle[26], M. Dreval[49], P. Drews[35], L. Dubus[23], R. Dumont[23], D. Dunai[24], M. Dunne[7], A. Durif[23], F. Durodie[38], G. Durr-Legoupil-Nicoud[5], B. Duval[5], R. Dux[7], T. Eich[7], A. Ekedahl[23], S. Elmore[1], G. Ericsson[19], J. Eriksson[19], B. Eriksson[19], F. Eriksson[1], S. Ertmer[35], A. Escarguel[22], B. Esposito[17], T. Estrada[28], E. Fable[7], M. Faitsch[7], N. Fakhrayi Mofrad[14], A. Fanni[27], T. Farley[1], M. Farnk[12], N. Fedorczak[23], F. Felici[5], X. Feng[50], J. Ferreira[39], D. Ferreira[39], N. Ferron[11], O. Fevrier[5], O. Ficker[12], A. R. Field[1], A. Figueiredo[39], N. Fil[1], D. Fiorucci[17], M. Firdaouss[23], R. Fischer[7], M. Fitzgerald[1], M. Flebbe[35], M. Fontana[1], J. Fontdecaba Climent[28], A. Frank[5], E. Fransson[51], L. Frassinetti[29], D. Frigione[42], S. Futatani[32], R. Futtersack[1], S. Gabriellini[52], D. Gadariya[28], D. Galassi[5], K. Galazka[44], J. Galdon[26], S. Galeani[42], D. Gallart[32], A. Gallo[23], C. Galperti[5], M. Gambrioli[11], S. Garavaglia[15], J. Garcia[23], M. Garcia Munoz[26], J. Gardarein[20], L. Garzotti[1], J. Gaspar[53], R. Gatto[52], P. Gaudio[42], M. Gelfusa[42], J. Gerardin[23], S. N. Gerasimov[1], R. Gerru Miguelanez[54], G. Gervasini[15], Z. Ghani[1], F. M. Ghezzi[15], G. Ghillardi[17], L. Giannone[7], S. Gibson[1], L. Gil[39], A. Gillgren[51], E. Giovannozzi[17], C. Giroud[1], G. Giruzzi[23], T. Gleiter[7], M. Gobbin[11], V. Goloborodko[55], A. González Ganzábal[28], T. Goodman[5], V. Gopakumar[1], G. Gorini[25], T. Görler[7], S. Gorno[5], G. Granucci[15], D. Greenhouse[3], G. Grenfell[7], M. Griener[7], W. Gromelski[44], M. Groth[14], O. Grover[7,12], M. Gruca[44], A. Gude[7], C. Guillemaut[23], R. Guirlet[23], J. Gunn[23], T. Gyergyek[46], L. Hagg[19], A. Hakola[10], J. Hall[16], C. J. Ham[1], M. Hamed[6], T. Happel[7], G. Harrer[56], J. Harrison[1], D. Harting[35], N. C. Hawkes[1], P. Heinrich[7], S. Henderson[1], P. Hennequin[57], R. Henriques[1], S. Heuraux[37], J. HidalgoSalaverri[26], J. Hillairet[23], J. C. Hillesheim[1], A. Hjalmarsson[19], A. Ho[6], J. Hobirk[7], E. Hodille[23], M. Hölzl[7], M. Hoppe[5,29], J. Horacek[12], N. Horsten[41], L. Horvath[1], M. Houry[23], K. Hromasova[12], J. Huang[35], Z. Huang[1], A. Huber[35], E. Huett[5], P. Huynh[23], A. Iantchenko[5], M. Imrisek[12], P. Innocente[11], C. Ionita Schrittwieser[58], H. Isliker[59], P. Ivanova[60], I. Ivanova Stanik[44], M. Jablczynska[44], A. S. Jacobsen[54], P. Jacquet[1], A. Jansen van Vuuren[5,26], A. Jardin[61], H. Järleblad[54], A. Järvinen[10], F. Jaulmes[12], T. Jensen[54], I. Jepu[1,47], S. Jessica[62], E. Joffrin[23], E. Joffrin[23], T. Johnson[29], A. Juven[23], J. Kalis[7], A. Kappatou[7], J. Karhunen[10], R. Karimov[5], A. N. Karpushov[5], S. Kasilov[13], Y. Kazakov[38], P. V. Kazantzidis[18], D. Keeling[1], W. Kernbichler[13], H. T. Kim[1], D. B. King[1], V. G. Kiptily[1], A. Kirjasuo[10], K. K. Kirov[1], A. Kirschner[35], A. Kit[63], T. Kiviniemi[14], F. Kjær[54], E. Klinkby[54], A. Knieps[35], U. Knoche[35], M. Kochan[43], F. Köchl[1], G. Kocsis[1], J. T. W. Koenders[6], L. Kogan[1], Y. Kolesnichenko[55], Y. Kominis[18], M. Komm[12], M. Kong[5], B. Kool[6], S. B. Korsholm[54], D. Kos[1], M. Koubiti[20], J. Kovacic[46], Y. Kovtun[49], E. Kowalska-Strzeciwilk[44], K. Koziol[64], M. Kozulia[49], A. Krämer Flecken[35], A. Kreter[35], K. Krieger[7], O. Krutkin[5], O. Kudlacek[7], U. Kumar[5], H. Kumpulainen[14], M. H. Kushoro[25], R. Kwiatkowski[64], M. La Matina[11], B. Labit[5], M. Lacquaniti[27], L. Laguardia[15], P. Lainer[13], P. Lang[7], M. Larsen[54], E. Laszynska[44], K. D. Lawson[1], A. Lazaros[18], E. Lazzaro[15], M. Y. K. Lee[5], S. Leerink[14], M. Lennholm[1], E. Lerche[38], Y. Liang[35], A. Lier[7], J. Likonen[10], O. Linder[7], B. Lipschultz[3], A. Listopad[5], X. Litaudon[23], E. LitherlandSmith[1], D. Liuzza[17], T. Loarer[23], P. J. Lomas[1], J. Lombardo[11], N. Lonigro[3], R. Lorenzini[11], C. Lowry[1], T. Luda di Cortemiglia[7], A. LudvigOsipov[51], T. Lunt[7], V. Lutsenko[55], E. Macusova[12], R. Mäenpää[14], P. Maget[23], C. F. Maggi[1], J. Mailloux[1], S. Makarov[7], K. Malinowski[44], P. Manas[23], A. Mancini[26], D. Mancini[5,40], P. Mantica[40], M. Mantsinen[65], J. Manyer[32], M. Maraschek[7], G. Marceca[5], G. Marcer[15], C. Marchetto[66], S. Marchioni[5], A. Mariani[15], M. Marin[5], M. Markl[13], T. Markovic[12], D. Marocco[17], S. Marsden[1], L. Martellucci[42], P. Martin[11], C. Martin[22], F. Martinelli[42], L. Martinelli[5], J. R. Martin-Solis[67], R. Martone[21], M. Maslov[1], R. Masocco[42], M. Mattei[21], G. F. Matthews[1], D. Matveev[35], E. Matveeva[12], M. L. Mayoral[1], D. Mazon[23], S. Mazzi[5,20], C. Mazzotta[17], G. McArdle[1], R. McDermott[7], K. McKay[26], A. G. Meigs[1], C. Meineri[30], A. Mele[40], V. Menkovski[2], S. Menmuir[1], A. Merle[5], H. Meyer[1], K. Mikszuta-Michalik[44], D. Milanesio[30], F. Militello[1], A. Milocco[25], I. G. Miron[47], J. Mitchell[1], R. Mitteau[23], V. Mitterauer[7], J. Mlynar[12],

V. Moiseenko[49], P. Molna[5], F. Mombelli[68], C. Monti[17], A. Montisci[27], J. Morales[23], P. Moreau[23], J. M. Moret[5], A. Moro[15], D. Moulton[1], P. Mulholland[2], M. Muraglia[20], A. Murari[11], A. Muraro[15], P. Muscente[11], D. Mykytchuk[5], F. Nabais[39], Y. Nakeva[40], F. Napoli[17], E. Nardon[23], M. F. Nave[39], R. D. Nem[54], A. Nielsen[54], S. K. Nielsen[54], M. Nocente[25], R. Nouailletas[23], S. Nowak[15], H. Nyström[29], R. Ochoukov[7], N. Offeddu[5], S. Olasz[24], C. Olde[1], F. Oliva[42], D. Oliveira[5], H. J. C. Oliver[1], P. Ollus[14], J. Ongena[38], F. P. Orsitto[17], N. Osborne[1], R. Otin[1], P. Oyola Dominguez[26], D. I. Palade[47], S. Palomba[42], O. Pan[7], N. Panadero[28], E. Panontin[25], A. Papadopoulos[18], P. Papagiannis[18], G. Papp[7], V. V. Parail[1], C. Pardanaud[20], J. Parisi[69], A. Parrott[1], K. Paschalidis[70], M. Passoni[68], F. Pastore[5], A. Patel[1], B. Patel[1], A. Pau[5], G. Pautasso[7], R. Pavlichenko[49], E. Pawelec[64], B. Pegourie[23], G. Pelka[44], E. Peluso[42], A. Perek[5,6], E. Perelli Cippo[15], C. Perez Von Thun[44], P. Petersson[29], G. Petravich[24], Y. Peysson[23], V. Piergotti[17], L. Pigatto[11], C. Piron[17], L. Piron[11], A. Pironti[21], F. Pisano[27], U. Plank[7], B. Ploeckl[7], V. Plyusnin[39], A. Podolnik[12], Y. Poels[2,5], G. Pokol[24], J. Poley[5], G. Por[24], M. Poradzinski[1], F. Porcelli[30], L. Porte[5], C. Possieri[42], A. Poulsen[54], I. Predebon[11], G. Pucella[17], M. Pueschel[6], P. Puglia[5], O. Putignano[25], T. Pütterich[7], V. Quadri[23], A. Quercia[21], M. Rabinski[64], L. Radovanovic[56], R. Ragona[54], H. Raj[5], M. Rasinski[35], J. Rasmussen[54], G. Ratta[28], S. Ratynskaia[70], R. Rayaprolu[35], M. Rebai[15], A. Redl[40], D. Rees[14], D. Refy[24], M. Reich[7], H. Reimerdes[5], B. C. G. Reman[54], O. Renders[41], C. Reux[23], D. Ricci[15], M. Richou[23], S. Rienacker[57], D. Rigamonti[15], F. Rigollet[53], F. G. Rimini[1,71], D. Ripamonti[15], N. Rispoli[15], N. Rivals[23], J. F. Rivero Rodriguez[26], C. Roach[1], G. Rocchi[17], S. Rode[35,36], P. Rodrigues[39], J. Romazanov[35], C. F. Romero Madrid[26], J. Rosato[20], R. Rossi[42], G. Rubino[17], J. Rueda Rueda[26], J. Ruiz Ruiz[69], P. Ryan[1], D. Ryan[1], S. Saarelma[1], R. Sabot[23], M. Salewski[54], A. Salmi[10], L. Sanchis[14], A. Sand[14], J. Santos[39], K. Särkimäki[7], M. Sassano[42], O. Sauter[5], G. Schettini[72], S. Schmuck[15], P. Schneider[7], N. Schoonheere[23], R. Schramm[7], R. Schrittwieser[58], C. Schuster[7], N. Schwarz[7], F. Sciortino[7], M. Scotto d'Abusco[23], S. Scully[1], A. Selce[15], L. Senni[17], M. Senstius[54], G. Sergienko[35], S. E. Sharapov[1], R. Sharma[1], A. Shaw[1], U. Sheikh[5], G. Sias[27], B. Sieglin[7], S. A. Silburn[1], C. Silva[39], A. Silva[39], D. Silvagni[7], B. Simmendefeldt Schmidt[54], L. Simons[5], J. Simpson[1], L. Singh[30], S. Sipilä[14], Y. Siusko[49], S. Smith[1], A. Snicker[10], E. R. Solano[28], V. Solokha[14], M. Sos[12], C. Sozzi[15], F. Spineanu[47], G. Spizzo[11], M. Spolaore[11], L. Spolladore[42], C. Srinivasan[1], A. Stagni[11], Z. Stancar[1], G. Stankunas[73], J. Stober[7], P. Strand[51], C. I. Stuart[1], F. Subba[30], G. Y. Sun[5], H. J. Sun[1], W. Suttrop[7], J. Svoboda[12], T. Szepesi[24], G. Szepesi[1], B. Tal[7], T. Tala[10], P. Tamain[23], G. Tardini[7], M. Tardocchi[15], D. Taylor[1], G. Telesca[44], A. Tenaglia[42], A. Terra[35], D. Terranova[11], D. Testa[5], C. Theiler[5], E. Tholerus[1], B. Thomas[1], E. Thoren[70], A. Thornton[1], A. Thrysoe[54], Q. Tichit[23], W. Tierens[7], A. Titarenko[74], P. Tolias[70], E. Tomasina[11], M. Tomes[12], E. Tonello[5,68], A. Tookey[1], M. Toscano Jiménez[26], C. Tsironis[18], E. Tsitrone[23], E. Tsitrone[23], C. Tsui[5,75], A. Tykhyy[55], M. Ugoletti[11], M. Usoltseva[7], D. F. Valcarcel[1], A. Valentini[54], M. Valisa[11], M. Vallar[5], M. Valovic[1], S. I. Valvis[18], M. van Berkel[6], D. Van Eester[38], S. Van Mulders[5], M. van Rossem[5], R. Vann[3], B. Vanovac[76], J. Valera Rodriguez[67], J. Varje[14], S. Vartanian[23], M. Vecsei[24], L. Velarde Gallardo[26], M. Veranda[11], T. Verdier[54], G. Verdoolaege[16], K. Verhaegh[1], L. Vermare[57], G. Verona Rinati[42], N. Vianello[11,77], J. Vicente[39], E. Viezzer[26], L. Vignitchouk[70], F. Villone[21], B. Vincent[5], P. Vincenzi[11], M. O. Vlad[47], G. Vogel[7], I. Voitsekhovitch[1], I. Voldiner[28], P. Vondracek[12], N. M. T. Vu[5], T. Vuoriheimo[63], C. Wade[50], E. Wang[35], T. Wauters[43], M. Weiland[7], H. Weisen[5,74], N. Wendler[44], D. Weston[1], A. Widdowson[1], S. Wiesen[35], M. Wiesenberger[54], T. Wijkamp[2], M. Willensdorfer[7], T. Wilson[1], M. Wischmeier[7], A. Wojenski[78], C. Wuethrich[5], I. Wyss[42], L. Xiang[1], S. Xu[35], D. Yadykin[51], Y. Yakovenko[55], H. Yang[23], V. Yanovskiy[12], R. Yi[35], B. Zaar[29], G. Zadvitskiy[12], L. Zakharov[63], P. Zanca[11], D. Zarzoso[20], Y. Zayachuk[1], J. Zebrowski[64], M. Zerbini[17], P. Zestanakis[18], B. Zimmermann[7], M. Zlobinski[35], A. Zohar[46], V. K. Zotta[52], X. Zou[23], M. Zuin[11], M. Zurita[5] & I. Zychor[64]

[12]Institute of Plasma Physics of the CAS, Prague 8, Czechia. [13]Graz University of Technology, Graz, Austria. [14]Aalto University, Aalto, Finland. [15]Institute for Plasma Science & Technology, CNR, Milan, Italy. [16]Dept. of Applied Physics, Ghent University, Ghent, Belgium. [17]ENEA, Fusion & Nuclear Safety Dept., C.R. Frascati, Frascati (RM), Italy. [18]National Technical University of Athens, Zografou, Greece. [19]Dept. of Physics & Astronomy, Uppsala University, Uppsala, Sweden. [20]Aix-Marseille Univ., CNRS, PIIM, UMR 7345, Marseille, France. [21]Consorzio CREATE, Naples, Italy. [22]Aix-Marseille Univ., CNRS, PIIM F-13397, Marseille, France. [23]IRFM-CEA, Centre de Cadarache, St-Paul-lez-Durance, France. [24]Centre for Energy Research, Budapest, Hungary. [25]University of Milano-Bicocca, Milan, Italy. [26]Universidad de Sevilla, Seville, Spain. [27]Dept. of Electrical & Electronic Engineering, University of Cagliari, Cagliari, Italy. [28]Laboratorio Nacional de Fusión, CIEMAT, Madrid, Spain. [29]Electromagnetic Engineering & Fusion Science, KTH Royal Institute of Technology, Stockholm, Sweden. [30]Politecnico di Torino, Turin, Italy. [31]Dip. di Ing. Elettrica Elettronica e Informatica, Univ. di Catania, Catania, Italy. [32]Barcelona Supercomputing Center, Barcelona, Spain. [33]Institut Jean Lamour, CNRS-Univ. de Lorraine, Vandoeuvre-lés-Nancy, France. [34]Institute of Nuclear Physics, Kraków, Poland. [35]Forschungszentrum Jülich, IEK-4 Plasmaphysik, Jülich, Germany. [36]Faculty of Math. & Natural Sciences, Heinrich Heine Univ. Düsseldorf, Düsseldorf, Germany. [37]Institut Jean Lamour, Univ. de Lorraine, Nancy, France. [38]Laboratory for Plasma Physics LPP-ERM/KMS, Brussels, Belgium. [39]Instituto de Plasmas e FusÃ£o Nuclear, IST-ULisboa, Lisbon, Portugal. [40]UniversitÃ degli Studi della Tuscia, DEIM, Viterbo, Italy. [41]KU Leuven, Dept. of Mechanical Engineering, Leuven, Belgium. [42]UniversitÃ di Roma Tor Vergata, Rome, Italy. [43]ITER Organization, St-Paul-lez-Durance Cedex, France. [44]Institute of Plasma Physics & Laser Microfusion, Warsaw, Poland. [45]Astrophysics Research Centre, Queen's University Belfast, Belfast, UK. [46]Jožef Stefan Institute & Univ. of Ljubljana, Ljubljana, Slovenia. [47]Nat. Inst. for Laser, Plasma & Radiation Physics, Măgurele, Romania. [48]Aix-Marseille Univ., CNRS, M2P2, Marseille, France. [49]Kharkov Inst. of Physics & Technology, Kharkiv, Ukraine. [50]Dept. of Physics, Durham University, Durham, UK. [51]Dept. of Space, Earth & Environment, Chalmers Univ. of Technology, Gothenburg, Sweden. [52]Dip. di Ing. Astronautica, Sapienza Univ. di Roma, Rome, Italy. [53]Aix-Marseille Univ., CNRS, IUSTI UMR 7343, Marseille, France. [54]Dept. of Physics, Technical Univ. of Denmark, Kongens Lyngby, Denmark. [55]Institute for Nuclear Research, Kyiv, Ukraine. [56]Technische Universität Wien, Vienna, Austria. [57]Laboratoire de Physique des Plasmas, École Polytechnique, Palaiseau, France. [58]Institute of Ion Physics & Applied Physics, Univ. of Innsbruck, Innsbruck, Austria. [59]Aristotle University of Thessaloniki, Thessaloniki, Greece. [60]Institute of Electronics, Bulgarian Academy of Sciences, Sofia, Bulgaria. [61]Institute of Nuclear Physics PAN, Kraków, Poland. [62]Loughborough University, Loughborough, UK. [63]University of Helsinki, Helsinki, Finland. [64]National Centre for Nuclear Research, Otwock-Åšwierk, Poland. [65]ICREA & Barcelona Supercomputing Center, Barcelona, Spain. [66]CNR & Dip. di Energia, Politecnico di Torino, Turin, Italy. [67]Universidad Carlos III de Madrid, Leganés, Spain. [68]Politecnico di Milano, Milan, Italy. [69]Rudolf Peierls Centre for Theoretical Physics, University of Oxford, Oxford, UK. [70]Space & Plasma Physics, EECS, KTH, Stockholm, Sweden. [71]EUROfusion PMU, Garching, Germany. [72]University Roma Tre, Rome, Italy. [73]Lithuanian Energy

Institute, Kaunas, Lithuania. [74]V. N. Karazin Kharkiv National University, Kharkiv, Ukraine. [75]Center for Energy Research, UC San Diego, La Jolla, CA, USA. [76]Plasma Science & Fusion Center, MIT, Cambridge, MA, USA. [77]Istituto per la Scienza e la Tecnologia dei Plasmi, CNR, Padova, Italy. [78]Warsaw University of Technology, Warsaw, Poland.

the MAST Upgrade Team

J. R. Harrison[1], A. Aboutaleb[79], S. Ahmed[80], M. Aljunid[1], S. Y. Allan[1], H. Anand[81], Y. Andrew[82], L. C. Appel[1], A. Ash[1], J. Ashton[1], O. Bachmann[1], M. Barnes[69], B. Barrett[1], D. Baver[83], D. Beckett[1], J. Bennett[1], J. Berkery[84], M. Bernert[7], W. Boeglin[79], C. Bowman[1], J. Bradley[4], D. Brida[7], P. K. Browning[85], D. Brunetti[1], P. Bryant[4], J. Bryant[4], J. Buchanan[1], N. Bulmer[1], A. Carruthers[1], M. Cecconello[50], Z. P. Chen[86], J. Clark[1,4], C. Cowley[3], M. Coy[1], N. Crocker[87], G. Cunningham[1], I. Cziegler[3], T. Da Assuncao[1], Y. Damizia[4], P. Davies[1], I. E. Day[1], G. L. Derks[2,6], S. Dixon[1], R. Doyle[8], M. Dreval[88], M. Dunne[7], B. P. Duval[5], T. Eagles[1], J. Edmond[1], H. El-Haroun[1], S. D. Elmore[1], Y. Enters[3], M. Faitsch[7], F. Federici[9], N. Fedorczak[23], F. Felici[5], A. R. Field[1], M. Fitzgerald[1], I. Fitzgerald[1], R. Fitzpatrick[86], L. Frassinetti[29], W. Fuller[89], D. Gahle[90], J. Galdon-Quiroga[26], L. Garzotti[1], S. Gee[1], T. Gheorghiu[3], S. Gibson[1], K. J. Gibson[3], C. Giroud[1], D. Greenhouse[3], V. H. Hall-Chen[88], C. J. Ham[1], R. Harrison[1], S. S. Henderson[1], C. Hickling[1,4], B. Hnat[89], L. Howlett[3], J. Hughes[76], R. Hussain[1], K. Imada[3], P. Jacquet[1], P. Jepson[1], B. Kandan[1], I. Katramados[1], Y. O. Kazakov[23], D. King[1], R. King[1], A. Kirk[1], M. Knolker[81], M. Kochan[1], L. Kogan[1], B. Kool[2,6], M. Kotschenreuther[89], M. Lees[1], A. W. Leonard[81], G. Liddiard[1], B. Lipschultz[3], Y. Q. Liu[81], B. A. Lomanowski[9], N. Lonigro[3], J. Lore[9], J. Lovell[9], S. Mahajan[86], F. Maiden[3], C. Man-Friel[1], F. Mansfield[1], S. Marsden[1], R. Martin[1], S. Mazzi[5], R. McAdams[1], G. McArdle[1], K. G. McClements[1], J. McClenaghan[81], D. McConville[1], K. McKay[4], C. McKnight[1], P. McKnight[1], A. McLean[91], B. F. McMillan[89], A. McShee[1], J. Measures[1], N. Mehay[1], C. A. Michael[89], F. Militello[1], D. Morbey[1], S. Mordijck[92], D. Moulton[1], O. Myatra[1], A. O. Nelson[93], M. Nicassio[1], M. G. O'Mullane[94], H. J. C. Oliver[1], P. Ollus[14], T. Osborne[81], N. Osborne[4], E. Parr[1], B. Parry[1], B. S. Patel[1], D. Payne[1], C. Paz-Soldan[93], A. Phelps[90], L. Piron[11,94], C. Piron[17], G. Prechel[94], M. Price[1], B. Pritchard[3], R. Proudfoot[1], H. Reimerdes[5], T. Rhodes[90], P. Richardson[1], J. Riquezes[93], J. F. Rivero-Rodriguez[1], C. M. Roach[1], M. Robson[1], K. Ronald[90], E. Rose[1], P. Ryan[1], D. Ryan[1], S. Saarelma[1], S. Sabbagh[93], R. Sarwar[1], P. Saunders[1], O. Sauter[5], R. Scannell[1], T. Schuett[3], R. Seath[1], R. Sharma[1], P. Shi[1], B. Sieglin[7], M. Simmonds[1], J. Smith[1], A. Smith[1], V. A. Soukhanovskii[91], D. Speirs[90], G. Staebler[81], R. Stephen[1], P. Stevenson[1], J. Stobbs[1], M. Stott[1], C. Stroud[1], C. Tame[1], C. Theiler[5], N. Thomas-Davies[1], A. J. Thornton[1], M. Tobin[93], M. Vallar[5], R. G. L. Vann[3], L. Velarde[26], K. Verhaegh[1], E. Viezzer[26], C. Vincent[1], G. Voss[1], M. Warr[1], W. Wehner[81], S. Wiesen[35], T. A. Wijkamp[2,6], D. Wilkins[1], T. Williams[1], T. Wilson[1], H. R. Wilson[3,9], H. Wong[87], M. Wood[1] & V. Zamkovska[93]

[79]Dept. of Physics, Florida International University, Miami, FL, USA. [80]Dept. of Physics & Technology, UiT The Arctic University of Norway, Tromsø, Norway. [81]General Atomics, San Diego, CA, USA. [82]Blackett Laboratory, Imperial College London, London, UK. [83]Astrodel LLC, Boulder, CO, USA. [84]Princeton Plasma Physics Laboratory, Princeton, NJ, USA. [85]Dept. of Physics & Astronomy, University of Manchester, Manchester, UK. [86]Institute for Fusion Studies, University of Texas at Austin, Austin, TX, USA. [87]Dept. of Physics & Astronomy, University of California Los Angeles, Los Angeles, CA, USA. [88]Institute of High Performance Computing, A*STAR, Singapore, Singapore. [89]Dept. of Physics, University of Warwick, Coventry, UK. [90]Dept. of Physics, SUPA, University of Strathclyde, Glasgow, UK. [91]Lawrence Livermore National Laboratory, Livermore, CA, USA. [92]Dept. of Computer Science, College of William & Mary, Williamsburg, VA, USA. [93]Dept. of Applied Physics & Applied Mathematics, Columbia University, New York, NY, USA. [94]University of California Irvine, Irvine, CA, USA.